

Numerical Analysis and Optimization of Wing-tip Designs

A project present to
The Faculty of the Department of Aerospace Engineering
San Jose State University

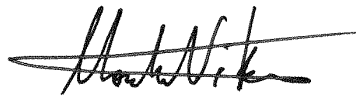
in partial fulfillment of the requirements for the degree
Master of Science in Aerospace Engineering

By

Uran Kim

May 2015

approved by



Dr. Nikos Mourtos
Faculty Advisor



© 2015

Uram Kim

ALL RIGHTS RESERVED

Numerical Analysis and Optimization of Wing-tip Designs

by

Uram Kim

APPROVED FOR THE DEPARTMENT OF AEROSPACE ENGINEERING

SAN JOSE STATE UNIVERSITY

May 2015



14 May 15

Dt. Nikos V. Mourtos, Project Advisor
Department of Aerospace Engineering

Date

ABSTRACT

NUMERICAL ANALYSIS AND OPTIMIZATION OF WING-TIP DESIGNS

By

Uram Kim

Vortex lattice method is used to optimize a winglet design for retrofitting a Boeing 747-100 wing. Parametric study involved 108 configurations corresponding to three different winglet airfoils, 6 winglet dihedral angles ranging from 7 to 90, and 6 toe-out angles ranging from 0 to -5. The optimized design features a Whitcomb winglet airfoil, 45° dihedral, and 0° toe-out, and is capable of reducing the induced drag by 12.5% in inviscid studies. Vortex lattice method, due to its limitations, is found to be incapable of capturing the toe-out effects of the winglets.

Compressible flow dynamics simulation in ESI is used to validate the optimized winglet design's effectiveness, but the lack of good understanding of turbulence modeling lead to the inability to converge a turbulence simulation to a good solution. The output of the CFD simulations do not support the performance of the winglet, but qualitative plots help to explain the physics of the flow past a wing and winglet.

ACKNOWLEDGEMENTS

I would like to thank my advisor and thesis mentor, Dr. Nikos Mourtos, for his support and guidance throughout the process of this study and my graduate school career at San Jose State University. I would also like to thank the CFD instructor, Ben Nikaido, for his support with the ESI software, as I was able to learn a lot about the software in a short time. Finally, I would like to thank my family, friends, and colleagues for their continuous support throughout my journey through higher education.

TABLE OF CONTENTS

| | |
|---|---------------------------|
| <u>Chapter 1 Introduction</u> | <u>8</u> |
| <u>Motivation and Objectives</u> | <u>8</u> |
| <u>Literature Review</u> | <u>11</u> |
| <u>Problem Description</u> | <u>18</u> |
| <u>Chapter 2 Computational Method Description</u> | <u>22</u> |
| <u>Athena Vortex Lattice Background</u> | <u>22</u> |
| <u>AVL Governing Equations</u> | <u>22</u> |
| <u>AVL Input/Output</u> | <u>27</u> |
| <u>ESI Background</u> | <u>28</u> |
| <u>Governing Equations</u> | <u>28</u> |
| <u>Grid Setup</u> | <u>29</u> |
| <u>Solver Setup</u> | <u>42</u> |
| <u>Chapter 3 Results</u> | <u>45</u> |
| <u>AVL Parametric Study</u> | <u>45</u> |
| <u>CFD Analysis</u> | <u>48</u> |
| <u>Chapter 4 Conclusion</u> | <u>60</u> |
| <u>References</u> | <u>61</u> |
| <u>Appendix</u> | <u>64</u> |

| | |
|--|---------------------------|
| <u>Modeled B747-100 Wing Geometry</u> | <u>64</u> |
| <u>Simulation Parameters at Steady Cruise</u> | <u>64</u> |
| <u>Airfoil Coordinates</u> | <u>64</u> |
| <u>Winglet design configurations based on varying dihedral angle</u> | <u>66</u> |
| <u>AVL Input File of B747-100</u> | <u>67</u> |
| <u>AVL Parametric Analysis Result</u> | <u>67</u> |

TABLE OF FIGURES

| | |
|---|----|
| Figure 1. Tip vortex generation | 9 |
| Figure 2. Various fuel saving wing-tip designs (KinneyJeremy, 2010) | 10 |
| Figure 3. Lanchester's winglet design (BargstenClayton, 2011) | 11 |
| Figure 4. Whitcomb's winglet design (WeiermanJacob & JacobJamey, 2010) | 13 |
| Figure 5. Illustration of the winglet toe-out angle (WeiermanJacob & JacobJamey, 2010) | 13 |
| Figure 6 Drag reduction of different wingtip devices (FayeRobert, LapreteRobert, WinterMichael, 2002) | 16 |
| Figure 7. Pareto front of optimal tip geometries | 17 |
| Figure 8. Boeing BACXXX Supercritical Airfoil | 19 |
| Figure 9. Whitcomb's results plotted against optimal design | 20 |
| Figure 10. Replacement of a finite wing with a bound vortex | 22 |
| Figure 11. Schematic of a lifting surface | 23 |
| Figure 12. AVL schematic | 25 |
| Figure 13. Trefftz Plane Analysis | 26 |
| Figure 14. Trefftz Plot | 27 |
| Figure 15. Airfoil coordinates shown as points in GEOM | 31 |
| Figure 16. C-grid geometry | 32 |
| Figure 17. C-grid defined by edges | 33 |
| Figure 18. Close up of edges around airfoil | 34 |
| Figure 19. Face from edges | 35 |
| Figure 20. Leading edge close up | 36 |

| | |
|--|---------------------------|
| <u>Figure 21. 3D mesh geometry setup</u> | <u>37</u> |
| <u>Figure 22. Wing-tip close up</u> | <u>38</u> |
| <u>Figure 23. Wing tip mesh nodes</u> | <u>39</u> |
| <u>Figure 24. Structured mesh faces</u> | <u>39</u> |
| <u>Figure 25. Cells in 3-D mesh</u> | <u>40</u> |
| <u>Figure 26. Internal view of layered mesh on the winglet</u> | <u>41</u> |
| <u>Figure 27. Layered C-grids on the wing with winglet</u> | <u>42</u> |
| <u>Figure 28. Winglet dihedral angle effect</u> | <u>46</u> |
| <u>Figure 29. Winglet toe-out angle effect</u> | <u>47</u> |
| <u>Figure 30. Unsuccessful turbulence simulation residual plot</u> | <u>49</u> |
| <u>Figure 31. Convergence history monitoring</u> | <u>50</u> |
| <u>Figure 32. Pressure contour at 0.5 m past base wing</u> | <u>52</u> |
| <u>Figure 33. Pressure contour at 3.5m past base wing</u> | <u>52</u> |
| <u>Figure 34. Streamlines past a base wing</u> | <u>53</u> |
| <u>Figure 35. Y+ contour plot on base wing surface</u> | <u>54</u> |
| <u>Figure 36. Convergence history of wing with winglet in turbulence</u> | <u>55</u> |
| <u>Figure 37. Y+ contour plot of winglet wing with turbulence</u> | <u>56</u> |
| <u>Figure 38. Pressure contour plot around the winglet with turbulence</u> | <u>56</u> |
| <u>Figure 39. Pressure contour plot around the trailing edge of winglet wing with turbulence</u> | <u>57</u> |
| <u>Figure 40. Y+ contour plot on the surface of winglet wing in laminar flow</u> | <u>58</u> |
| <u>Figure 41. Pressure contour plot 0.5m behind winglet in laminar flow</u> | <u>59</u> |
| <u>Figure 42. Pressure contour plot 3.5m behind winglet in laminar flow</u> | <u>59</u> |

TABLE OF TABLES

| | |
|---|---------------------------|
| <u>Table 1: Airfoil Comparison of AVL results</u> | <u>45</u> |
| <u>Table 2 CFD results summary</u> | <u>51</u> |

Chapter 1 Introduction

Motivation and Objectives

Since the beginning of the 21st century, there has been a large increase in the cost of petroleum. At the same time, there are growing concerns regarding the harmful effects of greenhouse gases on the earth's climate. Therefore, increasing the efficiency and reducing fuel consumption have been the primary goal of many transportation manufacturers, including the aviation industry.

A major portion of aircraft drag is due to vortex drag. Vortex drag is responsible for about 40% of the drag in cruise and about 80-90% of the drag in second segment climb. Vortex drag is caused by the tip vortices which occur in lifting wings. These tip vortices are generated at the tip of lifting wings and roll up as they move downstream as shown in figure 1 (ZhangH, ZhouY, WhitelawJ, 2006). The high pressure air from the bottom of the wing flows around the edge of the wing to the lower pressure region on top. The roll-up motion of the flow disrupts the lift generation at the tip of the wing and results in increased drag. Since the spiraling fluid flow of a vortex contains energy at the cost of reduced lift of the lifting wing, it is important to minimize induced drag of the wing tip vortices in order to improve performance and efficiency (NingS & KrooIIan, 2010).

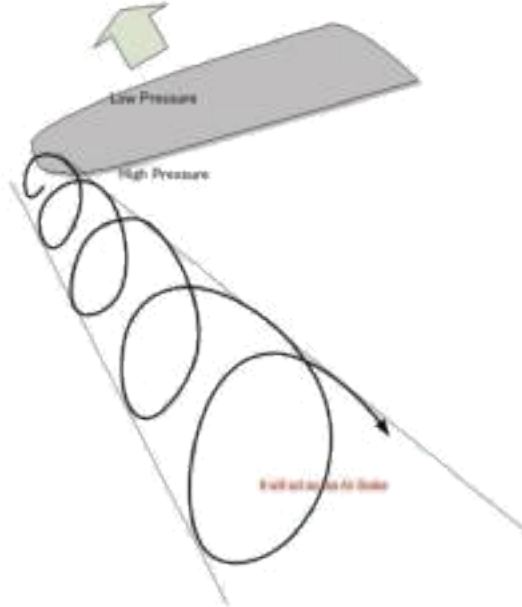


Figure 1. Tip vortex generation

Tip vortices are also powerful enough to introduce danger to smaller airplanes trailing a larger jetliner. The frequency of takeoffs at a given runway is limited by the dissipation time of vortices that aircrafts leave behind when they take off. A small aircraft can be flipped over if it encounters the tip vortices of a jumbo jet. For example, the crash of American Airlines flight 587 began with the smaller Airbus entering the trailing vortices of a jumbo jet after taking off immediately after a Boeing 747-400 (WaldMatthew & BakerAl, 2001). Because the vortices are generated at the wing tip, the wing tip geometry strongly affects vortex drag. It is necessary to develop new wingtip designs and retrofits that can either reduce the vortex intensity or move it away in relation to the aircraft longitudinal axis. Doing so will increase the effective span of the wing and therefore, reduce the vortex drag. From Sharklets to raked wingtips, different wing-tip designs have been implemented on different aircrafts in order to increase fuel efficiency of the aircrafts. Few examples of the recent designs are displayed in figure 2.

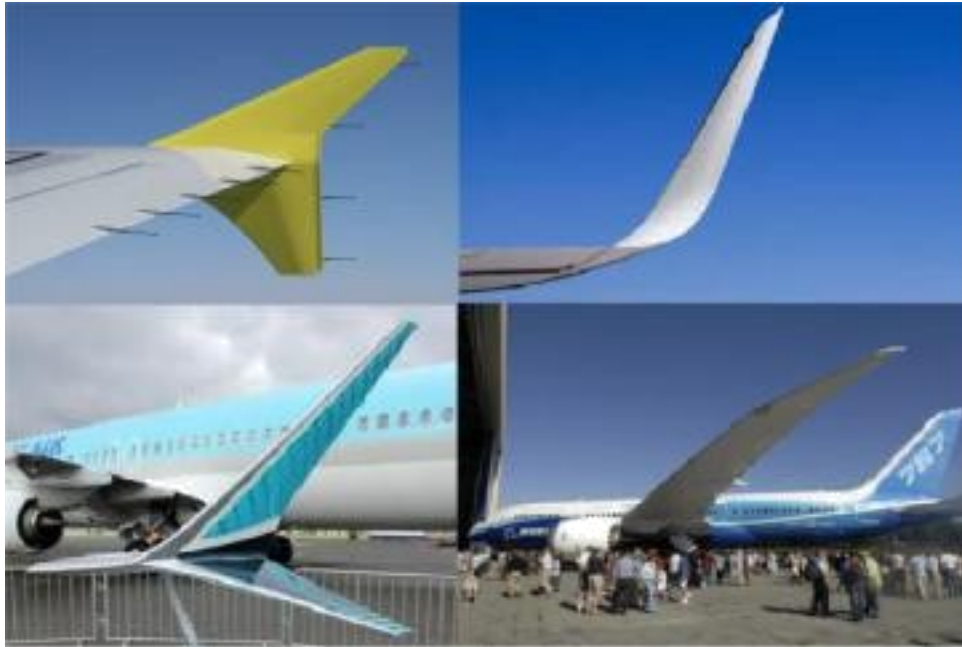


Figure 2. Various fuel saving wing-tip designs (KinneyJeremy, 2010)

The objective of this study is to develop and work through the process of optimizing a wing-tip design for retrofitting an existing aircraft and to compare the effectiveness of the optimized design to that of a commercial wing-tip design. This is achieved in three stages. First, detailed wing and wing-tip design of a designated aircraft is obtained. Having accurate description of the wing is a crucial step in achieving reliable CFD analysis. Next, a low fidelity parametric study is carried out in an inviscid flow analysis. This initial parametric study delivers an optimized wing-tip design which is further analyzed using CFD methods. High fidelity computational fluid dynamics analysis will output realistic aerodynamic loads which can be compared to that of existing wingtip designs to validate the design optimization.

Literature Review

The first studies on wingtip devices began even before the Wright brothers achieved their first flight. In 1917, English engineer Frederic Lanchester's research revealed that placing a vertical surface at the wingtip could reduce the wingtip drag. He called these places "endplates". As illustrated in Figure 3, these endplates mitigated the wingtip vortex formation by disrupting the flow from the bottom to the top of the wing. However, these flat plates created large flow separations and thus an increase in profile drag at cruise conditions (KinneyJeremy, 2010).

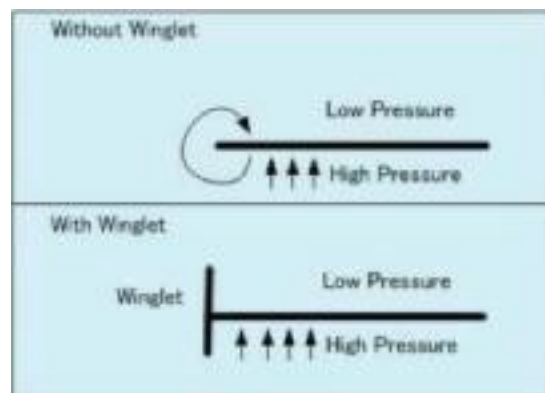


Figure 3. Lanchester's winglet design (BargstenClayton, 2011)

In 1952, a German aeronautical engineer, Dr. Sighard Hoerner developed a drooped wingtip design while he worked at the U.S. Wright-Patterson Air Force Base. These drooped wingtip design were used on gliders because they successfully increased the wing's overall lift-to-drag ratio by moving the vortex away from the wing's top. However, they were not very effective overall because the design created too much additional profile drag (KinneyJeremy, 2010).

After initial studies showed that certain wingtip designs can mitigate tip vortex generation, the work was cut out for scientists to come up with an effective design that is

practical. The first breakthrough came about at the hands of Richard Whitcomb in the 70s. With the OPEC oil embargo and resulting energy crisis, the pressure was on NASA to find ways of designing more efficient wings. Through the Aircraft Energy Efficiency program, Whitcomb experimented with wingtip designs for retrofitting a large twin engine aircraft and published a noteworthy report in 1976 which includes his optimized design geometry illustrated in figure 4. Whitcomb reported that the optimized wingtip design achieved 20% decrease in induced drag and 9% increase in lift-drag ratio compared to the baseline wing. The optimized design revealed that winglets should have a toe-out angle. The toe-out angle slants the incidence of the winglet away from the aircraft body. As figure 5 illustrates, the toe-out angle reorients the winglet lift force such that a component of the lift is pointed in the forward direction, providing a force similar to thrust and decreasing the overall drag. Also, Whitcomb compared the optimized winglet design to a simple wing-tip extension that results in similar structural impact by producing equivalent root bending moment of the wing. In the end, the winglet design was deemed superior as the optimized winglet delivered twice the lift-drag ratio increase as a simple tip extension (WhitcombRichard, 1976).

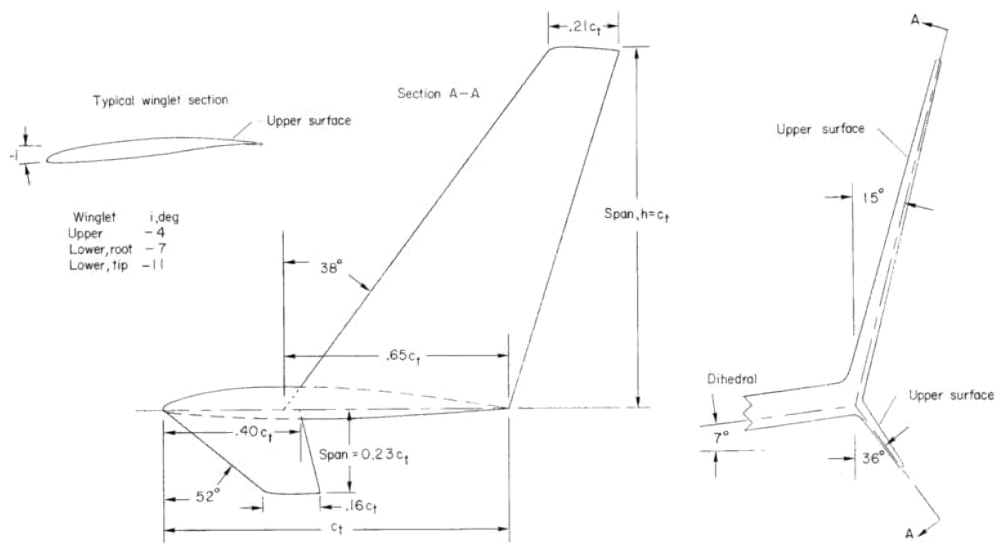


Figure 4. Whitcomb's winglet design (WeiermanJacob & JacobJamey, 2010)

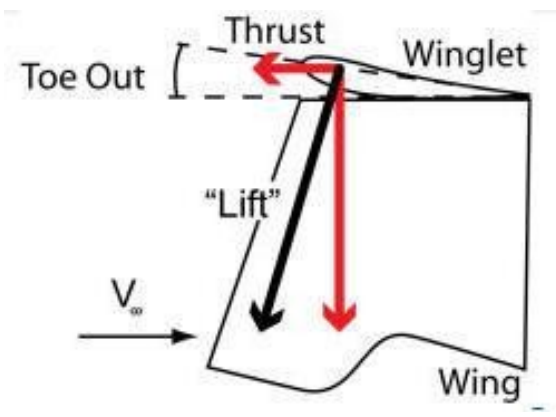


Figure 5. Illustration of the winglet toe-out angle (WeiermanJacob & JacobJamey, 2010)

At the heart of Whitcomb's research and all future development of winglet designs are wind tunnel experiments. Wind tunnels allow scientists to simulate the cruise condition of an aircraft in a small scale. Without having to build a large model and flying it, engineers can quickly gather preliminary data regarding a new design. This way, it is possible to design more successful prototypes. The rest of this discussion will review various wingtip designs that have

sprung from Whitcomb's winglet design and more contemporary designs based on wind tunnel experiments reported in literature.

Since circulation strength of a tip vortex is related to the lift loads near the wingtip, winglets are used most effectively on aircrafts with high lift. This is why winglets are widely used in high-altitude business jets and commercial airliners. The Boeing 747-400 was the first large U.S. commercial airliner to adopt the winglets in 1985. Boeing's winglet design resembled the Whitcomb winglets without the smaller winglet below the wingtip. Boeing decided to leave this part out in accommodation of ground-handling equipment. Overall, the winglets were found to bring 3 percent increase in efficiency (AllwardMaurice, 1989).

Airbus's wingtip design, called "wingtip fences", more closely resembled the Whitcomb winglets. Instead of a 90 degree extension at the tip of the wing, the wingtip fences extended both above and below the wingtips in a "V" shape. This design was developed by the British and first installed in 1985 on the A310-300. Airbus reported a fuel savings of almost 5 percent with this winglet installation (BargstenClayton, 2011).

To cope with the rising Boeing retrofitted over 2,500 jets with blended winglets by 2003. Blended winglets make a smooth transition between the winglet and the wing to avoid interference drag from a sharp angle at the wing-winglet junction. Such sharp angle at the junction can interact with the boundary layer flow and cause a drag induced vortex, negating some of the benefits of the winglet. In 2009 Airbus started their own blended winglet design, "sharklet", to be used in the new A320 aircrafts. Study showed that blended winglets can result in at least 3.5 percent reduction in fuel burn (Airbus, 2009).

One of the newest wingtip designs is the raked wingtips used on the new Boeing 787 and 747-8. The Boeing Company and NASA developed this design from various wind tunnel tests which gave them a better understanding of how wingtips work. In a raked wingtip design, the tip of the wing has higher degree of sweep than the rest of the wing. By doing so, wingtip vortex generation is mitigated, and the effective aspect ratio of the wing can be increased, leading to increased efficiency, improved climb performance, and shorter takeoff distance. This technology is expected to bring at least 6 percent increase in range (YoonJoe, 2003).

Different aircrafts use different wingtip designs based on the specific situation and the aircrafts' aerodynamics. The graph below compares the effectiveness of different wingtip designs in reducing induced drag. Four different designs on five aircrafts are analyzed. While the only modification to KC- 135's wing is a winglet, the wings of MD-11 and 747-400 have gone through span increase and winglet installations. The 737 has gone through a more modern retrofit through the blended winglet, and the 767 boasts the newest of the designs with its raked wing tips.

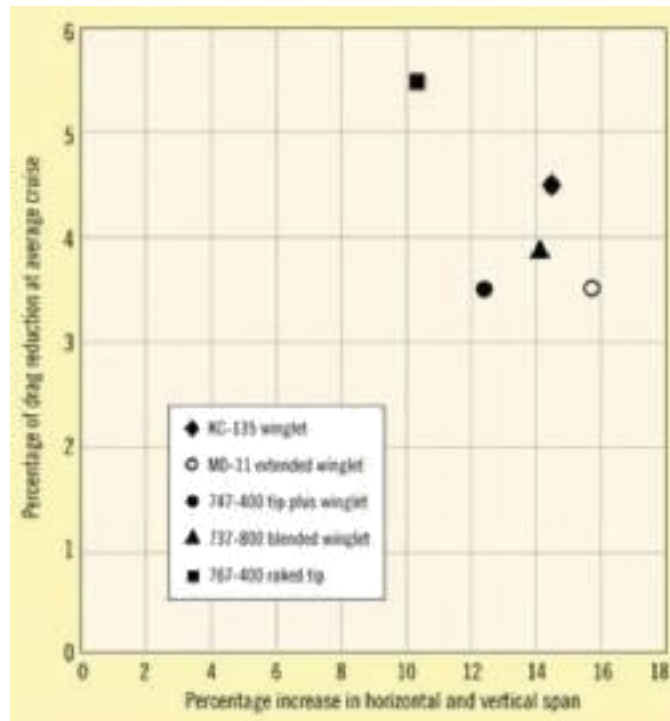


Figure 6 Drag reduction of different wingtip devices (FayeRobert, LapreteRobert, WinterMichael, 2002)

The resulting drag reduction of the four aircrafts with winglets are all around 4 percent. They suffer a larger percentage increase in vertical span due to the winglets stretching upward. The raked wing tip on the other hand clearly shows superiority over the winglets with its 5.5 percent reduction in drag. Also, because the raked wing tip only requires a modification in the horizontal span of the wing, the percentage increase in span is much lower than that of the winglet designs. Furthermore, in a winglet modeling project done at the Virginia Tech University, aerodynamic analysis using the Tornado VLM revealed up to 20% reduction in drag on wings with winglets compared to wings without (ShaferD, PemridgeJ, reillyM, 2004).

More recently, there have been many studies on the numerical optimization of different wingtip designs. One such study conducted at Stanford University takes into consideration the

consequential weight increase due to the addition of a wingtip design. It is remember to consider that there is a trade-off to retrofitting a wing with a wingtip design. Even though the induced drag is reduced with the addition of a wingtip design, the additional component adds to the aircraft's profile drag and skin friction drag. Furthermore, not only is there additional mass from the extra component, but even more weight increase results from the extra material necessary to support the structural loading caused by the wingtip design. Adding a wingtip design adds to two components of the wing weight: the load dependent weight which is proportional to the weight of the material used to resist the extra bending loads caused by the wingtip design and the area-dependent weight which is proportional to the additional wing area of the wingtip design. The numerical optimization study done by Ning and other at Stanford University revealed optimized span lengths of and drag reduction of a wingtip design based on the weight increase and the winglet dihedral angle. Figure 7 summarizes the findings.

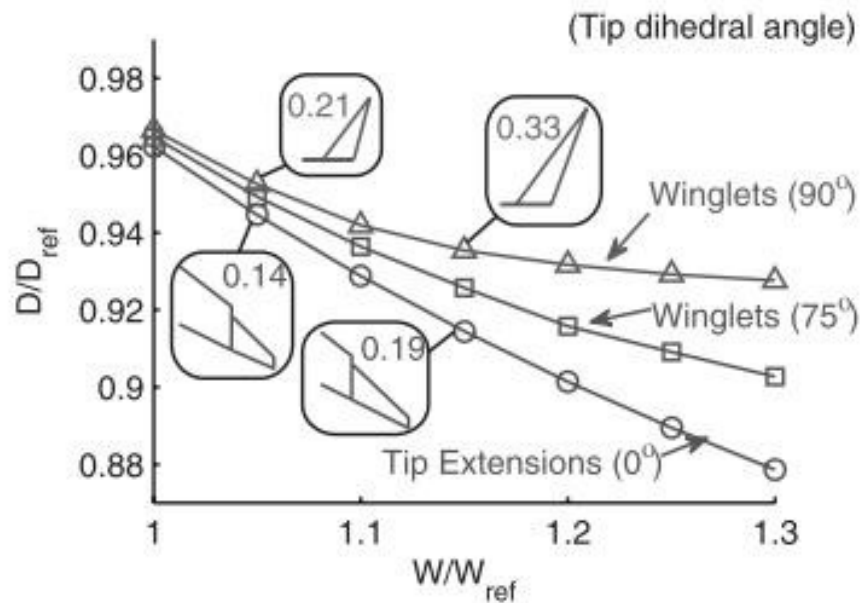


Figure 7. Pareto front of optimal tip geometries

The drag considered in this case includes viscous and vortex drag, but neglects wave drag at transonic speed. Note that depending on the dihedral angle, a wingtip design is labeled as a tip extension or a winglet. Unlike the Whitcomb study, the tip extension is preferred over a winglet in this numerical optimization (NingS & KrooIIan, 2010).

Problem Description

The aircraft chosen to be retrofit through this analysis is the Boeing 747. It is an iconic aircraft that kick started intercontinental air travel in the 70s. Due to its long cruise range, reducing the induced drag at cruise condition leads to significant improvement in its efficiency and range. The wing of the original 747-100 is used as the base model. The performance of the wing plus optimized wingtip design combo will be compared against that of the base model. Boeing 747's cruise velocity of Mach 0.84 at 35000 feet altitude corresponds to a lift coefficient C_L of 0.47 which was kept constant in the analysis in order to simulate identical flight conditions for all analyzed wings (Boeing, 2015).

A challenge to this study is that the detailed description of the 747 wing is proprietary information since the aircraft is still in service today. In order to model the wing, assumptions were made to simplify the wing geometry. First the base wing features one constant taper and no twist throughout the wing, instead of the actual wing which features twists and changing taper ratio throughout the wingspan. It was not possible to obtain the coordinates of the unique airfoils used on different sections of the wing, so Boeing's supercritical airfoil BACXXX, illustrated

below, was used as the constant airfoil throughout the wing (BOEING BACXXX AIRFOIL (bacxxx-il), 2015). Detailed geometry of the base wing is in the appendix.

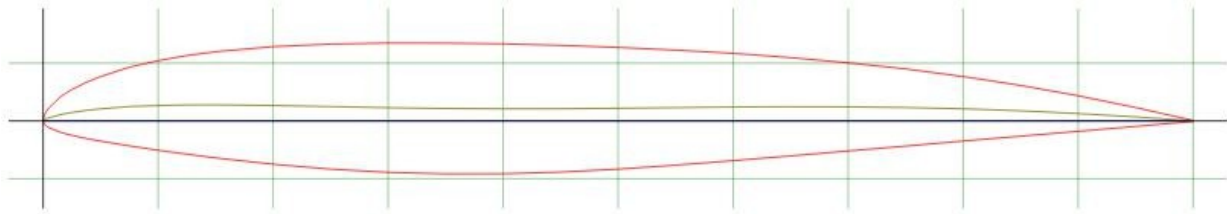


Figure 8. Boeing BACXXX Supercritical Airfoil

Low fidelity parametric analyses were performed on Athena vortex Lattice (AVL) which utilizes vortex lattice method to calculate the aerodynamic properties of a three-dimensional wing. Since there are so many geometric variables that define a wingtip design, it is important to first define the control variables before conducting a parametric study. Since the Whitcomb's optimization was done for retrofitting a large twin engine aircraft similar to the Boeing 747, his study was referenced to set up the parametric study. The figure below compares the results of Whitcomb's study against the Pareto fronts defined by Ning's numerical optimization mentioned above.

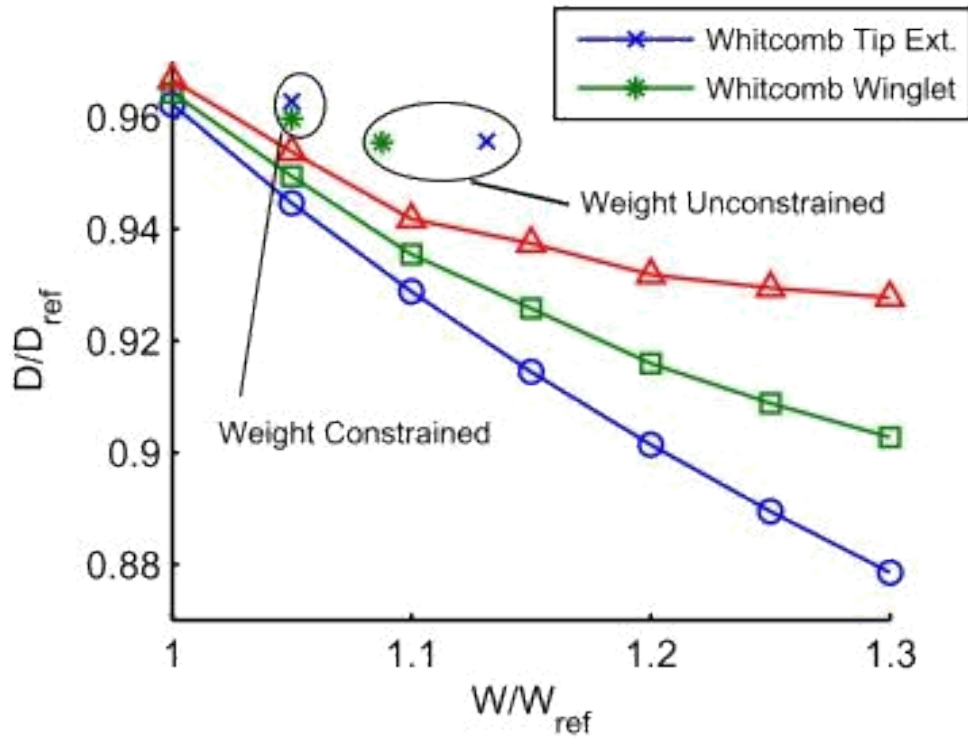


Figure 9. Whitcomb's results plotted against optimal design

In order for a proper comparison with both the Whitcomb and Ning's findings, 5% weight increase constraint was placed on all of the wingtip designs. Based on the weight constraint, the optimal span increase for a given dihedral angle was used for each wingtip design, ranging from 0.14 to 0.21 of the base wing span. These designs are expected to bring about 5% decrease in viscous and vortex drag (NingS & KrooIIan, 2010). For the root chord length, tip chord length, taper, location, and sweep of the wingtip design, Whitcomb's optimized upper winglet shown in figure 4 was used.

After defining the control variables, the ranges for variables of interest were defined to finish the parametric study setup. First of all, the wingtip dihedral angle was varied in six

configurations from 7° , corresponding to a tip extension, to 90° , which corresponds to a vertical winglet. Many optimization studies have been done on wingtip designs with dihedral angles near vertical or horizontal, but there aren't many previous studies on the wingtip designs with dihedral angles between the two most popular designs. Next, the toe out angle of the wingtip was varied between 0° and -5° in six configurations. The purpose of this was to find the optimal angle that allows the wingtip design to provide the most thrust forward. Finally, three airfoils were used on the wingtip designs. The first configuration was to design the wingtip with the same airfoil as the base wing. Since the wingtip faces the same freestream as the rest of the wing, the Boeing supercritical airfoil is acceptable for the wingtip as well. Second, the Whitcomb airfoil, illustrated below, was used. This is the airfoil designed by Whitcomb and used in his optimization study. Lastly, a sailplane winglet airfoil, PSU-90-125WL, was used. This relatively thick airfoil was expected to bring higher lift than the other airfoils used in the study. In summary, there were 36 test cases per airfoil, 108 in total.

From the inviscid parametric analysis, the optimized design was determined by finding the configuration with most reduced induced drag. This design is, then, modeled as a 3-D wing and analyzed via computational fluid dynamics alongside the base wing. For CFD study which includes viscous flow, ESI software is used. The aerodynamic load outputs and the qualitative plots will confirm the effectiveness of the design optimization. The coordinates of the airfoils, analysis parameters for CFD and AVL, and the detailed geometry of the wingtip designs based on varying dihedral angle are in the appendix.

Chapter 2 Computational Method Description

Athena Vortex Lattice Background

The data for the study was gathered from an AVL generated Trefftz Plane Plot which contains information such as angle of attack, lift coefficient, drag coefficient, and Oswald's efficiency. AVL is only valid for inviscid flow, and therefore the drag coefficient is from induced drag due to lift. This means that compressibility effects, viscous effects, and boundary layers are not considered in this study.

AVL Governing Equations

According to Prandtl's classical lifting-line theory, it is possible to model a finite wing with a horseshoe vortex which consists of a bound vortex line with free-trailing vortex lines on either side as shown in figure 10.

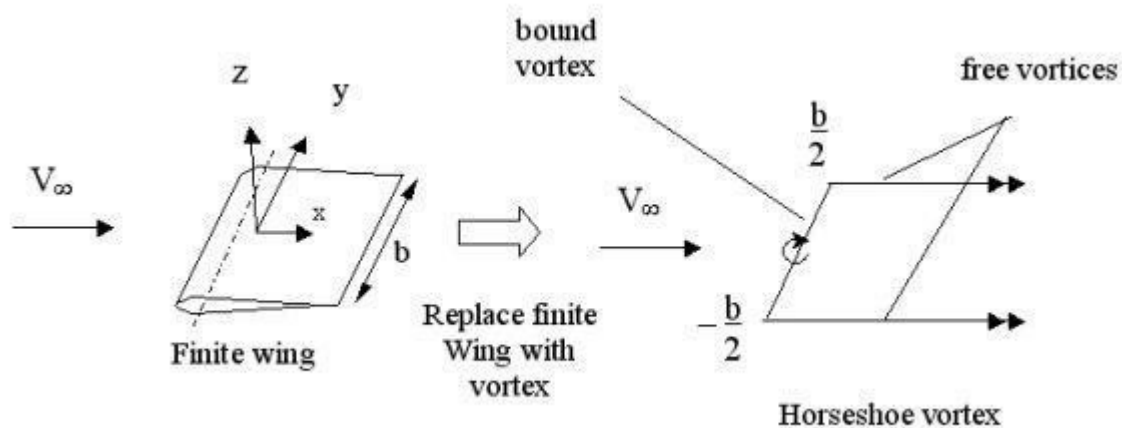


Figure 10. Replacement of a finite wing with a bound vortex

If the origin is taken at the center of the bound vortex, then the velocity at any point along the bound vortex induced by the trailing semi-infinite vortices is,

$$v = \frac{\Gamma}{4\pi z}$$

Equation 1

For a more sophisticated modeling of a three dimensional wing, this model can be extended by placing a series of lifting lines on the surface of the wing. It is possible to form a vortex sheet to model the wing by placing a large number of lifting lines all parallel to the y axis, located at different values of x as shown in figure 11.

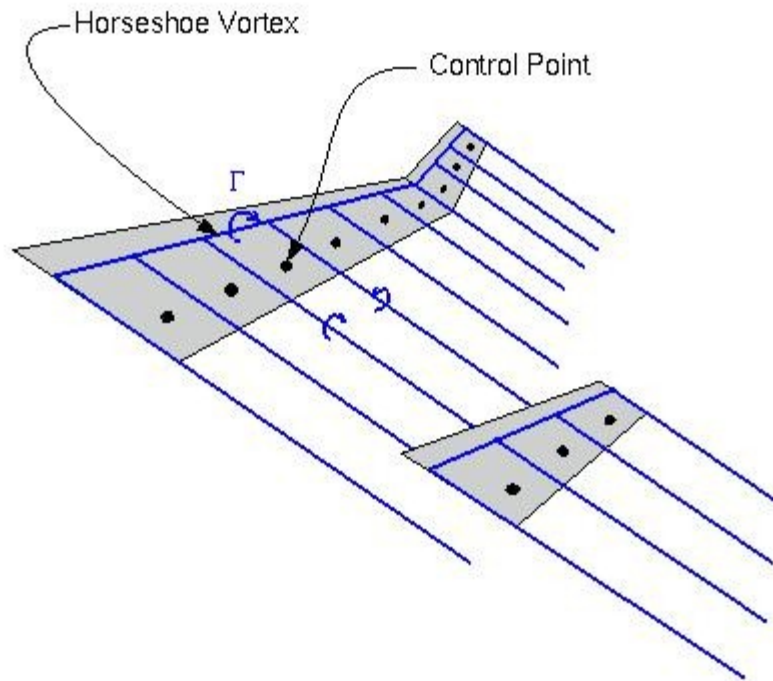


Figure 11. Schematic of a lifting surface

With this setup, the normal velocity induced at a point P by both the lifting surface and the wake is

$$w(x, y) = - \frac{1}{4} \iint \frac{(\xi - x)(\eta - y) + (\xi - x)(\eta + y)}{4^2 [(x - \xi)^2 + (y - \eta)^2]^{3/2}}$$

Equation 2

The key to solving the lifting-surface theory is to solve the above equation for the spanwise vortex strength distribution $\gamma(\xi, \eta)$ and chordwise vortex strength distribution $\delta(\xi, \eta)$ so that the sum of $w(x, y)$ and the normal component of the freestream is zero. The evaluation of the equation at chosen control points for each panel results in a system of simultaneous algebraic equations that can be solved for the values of the vortex strength distribution on all the panels. Knowing the vortex strength distribution allows one to calculate the lift distribution by integrating the circulation Γ along the span as the following equation suggests.

$$L = \rho U \int_{-a}^a \Gamma dy$$

Equation 3

Athena Vortex Lattice (AVL) is a software developed at MIT for the purpose of analyzing a 3-dimensional flying body using the vortex panel method described above. It is important to note that the method's important assumptions are that the flow is incompressible, inviscid, and irrotational. Figure 12 illustrates a typical panel setup in AVL. The purple lines

represent the bound vortex lines, and the dotted white lines are the trailing vortices. The yellow dots are the control points.

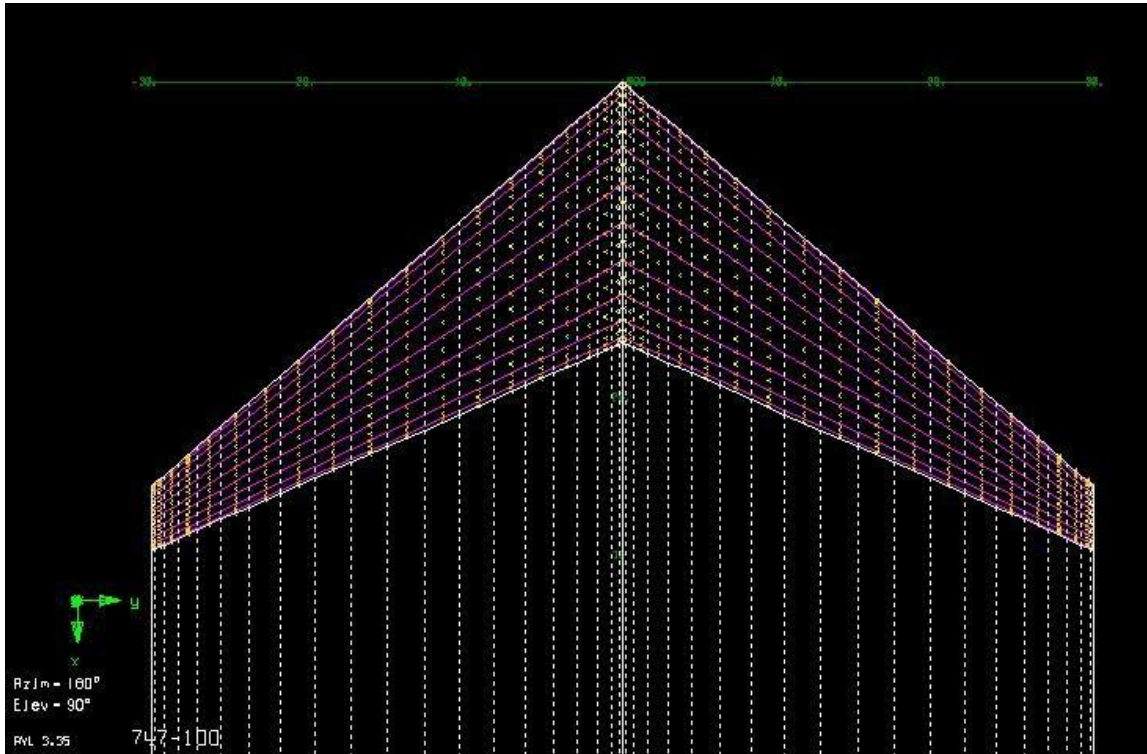


Figure 12. AVL schematic

An important function of AVL is the Trefftz Plot whose main point is to show the downwash angle measured at the Trefftz Plane which is a plane located at an infinite distance downstream of the wing, perpendicular to the wake. Consider the control volume surrounding the lifting body as shown in Figure 13.

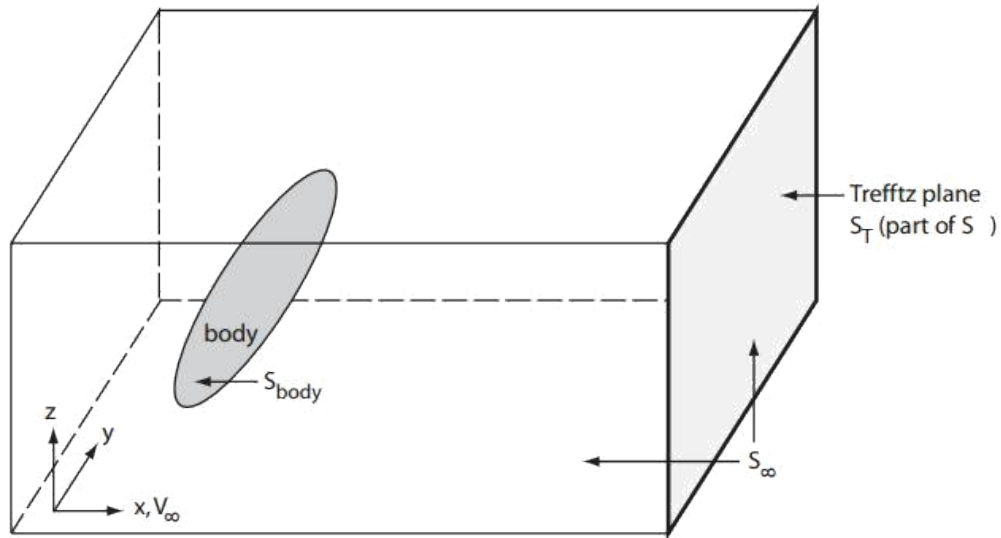


Figure 13. Trefftz Plane Analysis

Below is the momentum integral that can be applied to this control volume.

$$\iint_{S_{body}} \rho \mathbf{v} \cdot \mathbf{n} \, dS = - \iint_{S_{\infty}} \rho \mathbf{v} \cdot \mathbf{n} \, dS$$

Equation 4

At the Trefftz Plane, the Bernoulli's equation can be applied to the integral to calculate the induced drag coefficient in terms of the downwash angle.

$$\rho \int_{S_T} \mathbf{v} \cdot \mathbf{n} \, dS = \rho \int_{S_T} \mathbf{v} \cdot \mathbf{n} \, dS$$

Equation 5

Figure 14 shows a typical Trefftz Plot analysis in AVL. Along with the downwash angle distribution in blue, many other relevant parameters are also displayed such as the lift

distribution in green, the angle of attack α , the wing's lift coefficient C_L , and the wing's induced drag C_{Di} .

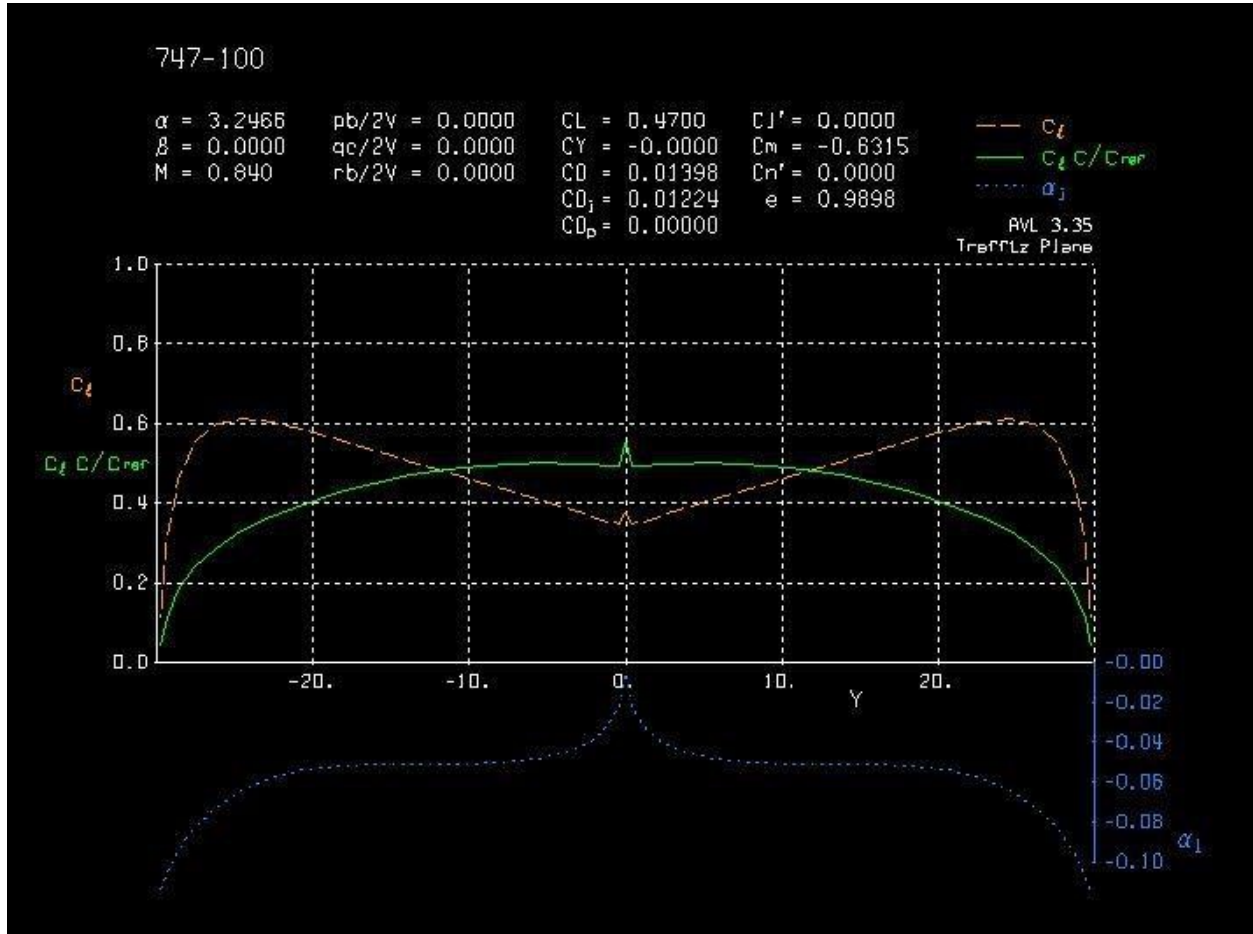


Figure 14. Trefftz Plot

AVL Input/Output

In order to execute calculations on AVL, the geometry of the wing or aircraft must be defined by creating and importing to AVL a text file with .avl extension. The input file that describes the geometry of the base wing is in the appendix. Once the calculation is made, the

angle of attack required to achieve the lift coefficient of 0.47 and the induced drag coefficient is obtained from the Trefftz Plot. The results from the parametric analysis is in the appendix.

ESI Background

For CFD analysis, ESI CFD Suite is used because it is readily available for the aerospace engineering students at SJSU. From the suite, the specific software used are CFD-GEOM, CFD-FASTRAN, and CFD-VIEW. CFD-GEOM is used to model the physical and the computational space, or mesh, of the problem at hand. Once the mesh is finished, the mesh file is imported into CFD-FASTRAN, which is a density based solver. Here, user can setup the input parameters and boundary conditions and start the model simulation. Once the simulation converges to a solution, the output force file can be viewed to obtain the calculated values for user-specified variables.

Also, the model solution can be imported to CFD-VIEW for post-processing. CFD-VIEW allows graphical representation of the simulation solution. Qualitative plots can be obtained from CFD-VIEW (CFD-FASTRAN V2014.0 User Manual, 2014).

Governing Equations

The governing equations of the high-fidelity CFD simulations are the Navier-Stokes set of equations which describe the motion of a viscous, heat conducting, and compressible fluid (LiepmannH, RothkoA, LindsayR, 1957). These equations allow a mathematical model of a gas as a continuum. Out of the three Navier-Stokes equations, the momentum equation in Equation 6 is the primary equation. Mass conservation, also known as continuity equation, is Equation 7 and the energy equation is Equation 8.

$$\frac{\partial}{\partial t} (\rho u_i) + \frac{\partial}{\partial x_j} (\rho u_i u_j) = -\frac{\partial p}{\partial x_i} + \frac{\partial}{\partial x_j} (\mu \frac{\partial u_i}{\partial x_j}) + \rho g_i, A_i = \dots = \dots$$

Equation 6

In the conservation of momentum equation above, the right hand side is responsible for modeling viscous flows. The right side is omitted when an inviscid flow is analyzed. Also, the k term is omitted when the modeled flow is laminar.

$$\frac{\partial}{\partial x_j} (\rho u_j) = 0$$

Equation 7

In the general continuity equation above, ρ is the mixture density and u_i is the mass averaged velocity in the x_i direction. This mass conservation equation is necessary for modeling a calorically perfect gas.

$$\frac{\partial}{\partial t} (\rho) + \frac{\partial}{\partial x_j} (\rho u_j) = 0$$

Equation 8

CFD softwares analyze these equations using a flow model that assumes a fluid moving through an infinitesimal fluid element fixed in space. (CFD-FASTAN V2014.0 User Manual, 2014).

Grid Setup

All CFD processes begin with a computational domain represented by a collection of cells called a mesh or grid. With ESI's meshing tool, CFD-GEOM, CAD-like tools are used to create the geometry of the model. The mesh and computational domain is generated by

discretizing the physical space into several cells once the geometry is created. CFD-GEOM builds the mesh from the nodes of the geometry.

There are two types of meshes: structured and unstructured. A mesh is structured when the connectivity between cells is built with the position of the nodes orderly stored in an array. Structured meshes require more manual effort than unstructured meshes in regards to setting up the geometry before a proper computational domain can be created due to the topology constraint. A structured mesh delivers a more accurate solution faster than a similar unstructured mesh with similar resolution because it requires less cells to analyze.

Grid spacing determines the model's resolution at the airfoil surface and therefore is critical to performing an accurate analysis. A well-defined grid will resolve the flow physics regarding flow separation on the upper airfoil surface. The distance from the wall to the first grid line of the mesh is a function of the y^+ value, which defines how coarse or fine a mesh is for given turbulent conditions. A large y^+ value is computed for turbulent flow and high Reynolds numbers (Compute Grid Spacing for a Given Y^+ , 2015). This dimensionless quantity describes drag induced by viscosity. In order to appropriately resolve the flow conditions in a turbulent simulation the initial grid spacing from the airfoil wall must have a y^+ of 1 or less. Boeing 747's cruise condition translates to an initial grid spacing (Δy) of $5E-06$ meters. The calculated Δy allowed for acceptable resolution into the flow in the boundary layer.

Meshing an airfoil starts by importing the airfoil coordinates into GOEM via tabulated XYZ data file (.tab) as shown in figure 15.

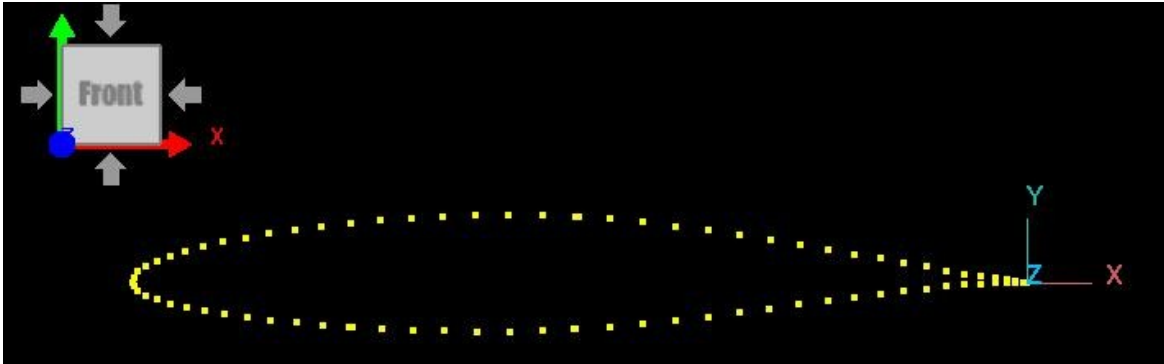


Figure 15. Airfoil coordinates shown as points in GEOM

After representing the upper and lower surfaces of the airfoil with curved lines, the outer bounds of the computational is defined with lines and points as illustrated in figure 16. The outer bounds are at least 10 chord lengths away from the airfoil, and this allows the freestream flow to be resolved without the effects of flow over the airfoil. This type of C-grid is typical of an airfoil simulation setup.

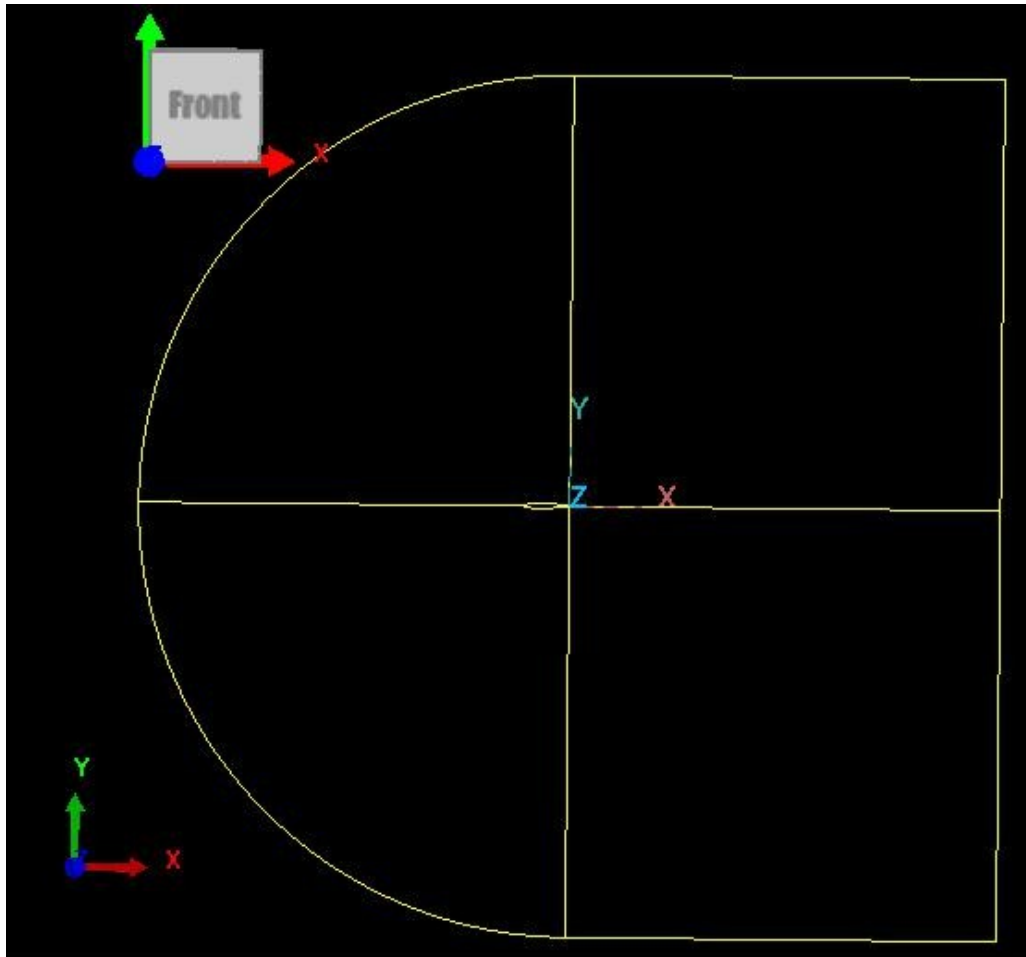


Figure 16. C-grid geometry

Once the basic geometry is created, the nodes need to be placed in order to define the computational space. The nodes are placed by creating edges on existing lines. For this analysis, 100 grid points were placed per edge segment as shown in figure 17.

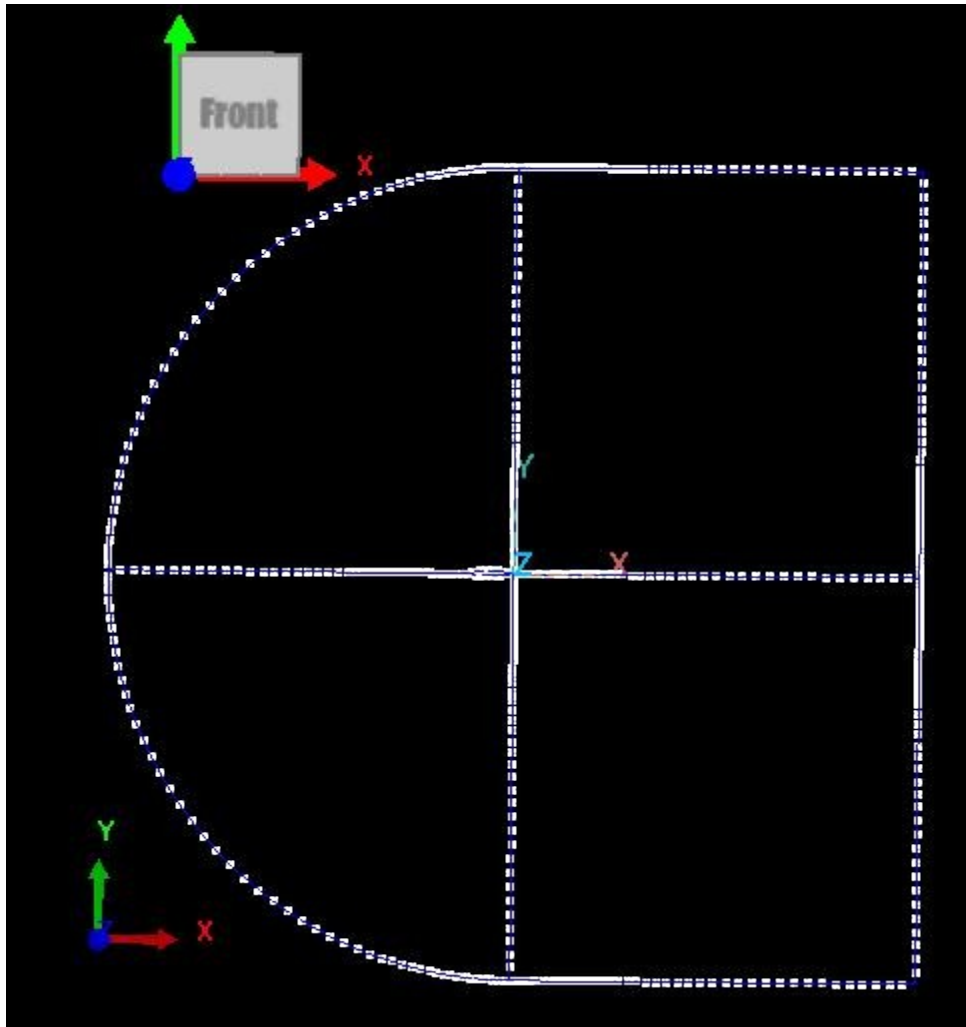


Figure 17. C-grid defined by edges.

Closer inspection of the airfoil edges in figure 18 reveal that higher concentration of the grid points were placed on the leading and trailing edges of the airfoil. This is to achieve higher resolution of computation at locations that involve greater change to fluid element. The minimum spacing of grid points used at leading and trailing edges is 0.005 m.

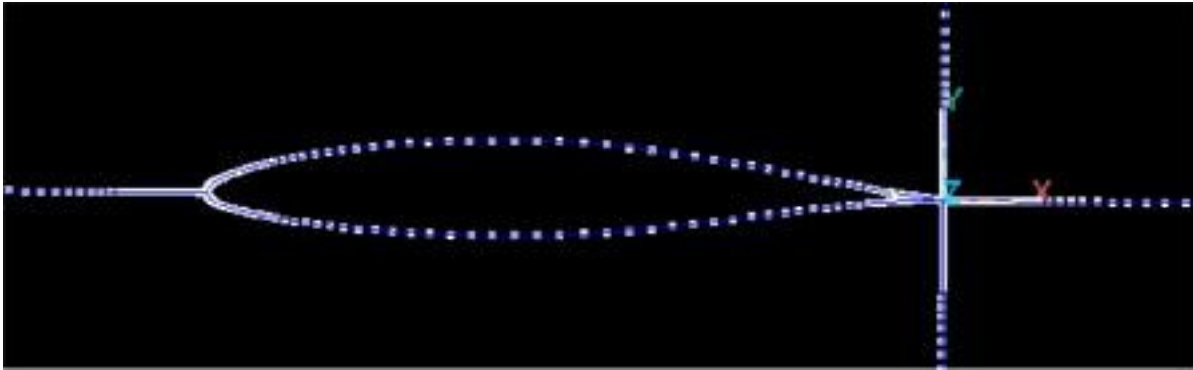


Figure 18. Close up of edges around airfoil.

The minimum grid spacing of the vertical edges at airfoil trailing edge represent minimum size of the cells at the airfoil surface. In a viscous flow, there exists a boundary layer on an object's surface as the flow velocity on the surface is zero and gradually speeds up to reference velocity further away from the surface. In order to adequately capture the boundary layer of an object, it is necessary to achieve y^+ value of 1 or less on the object's surface. An online y^+ calculator is used to calculate the grid spacing necessary in order to achieve y^+ of 1 (Compute Grid Spacing for a Given Y^+ , 2015). The y^+ value is dependent on freestream velocity, density, dynamic viscosity, and reference length. The lower the y^+ value, the smaller the initial grid spacing required.

Using the edges, faces can be formed to define the individual cells of the structured mesh. As illustrated in figure 19, it takes 4 sets of edges to form one face.

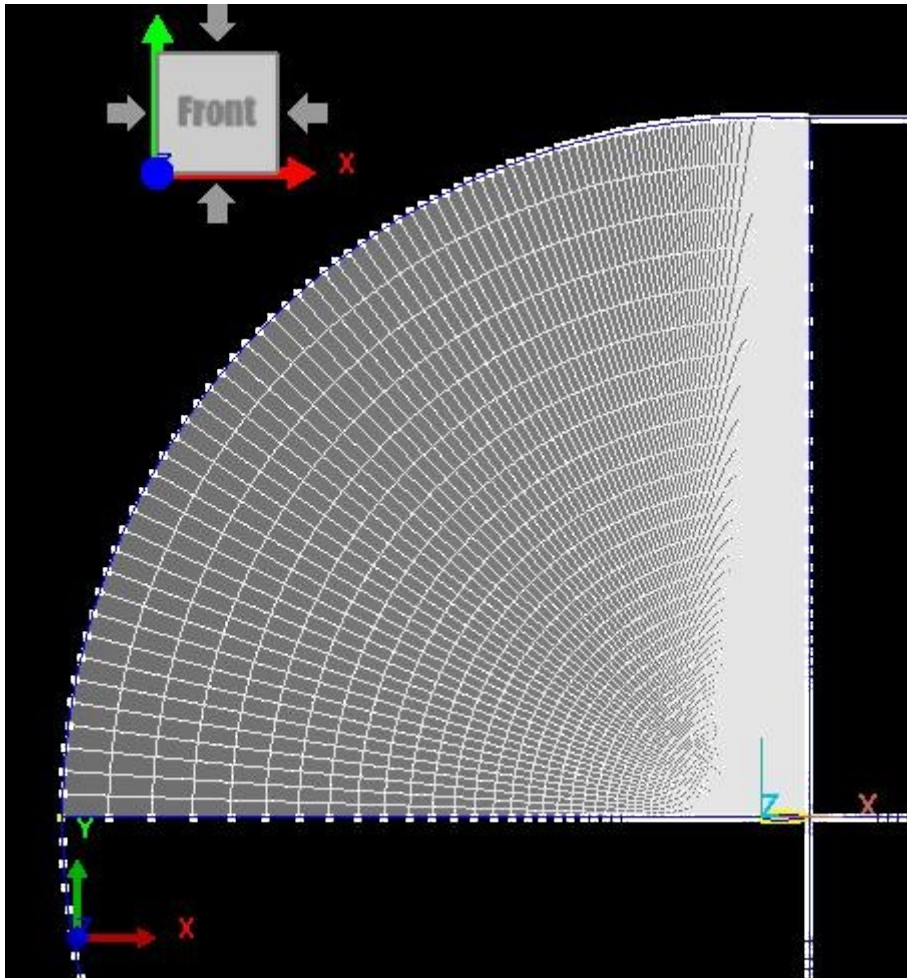


Figure 19. Face from edges.

At this point, it is important to adjust the spacing of the far field grid spacing and use the face smoothing function of GEOM in order to achieve orthogonality of the cell boundaries coming out of the airfoil surface grid points as shown in figure 20. More regularly sized cells and straighter cell boundaries allow faster convergence to more accurate solution.

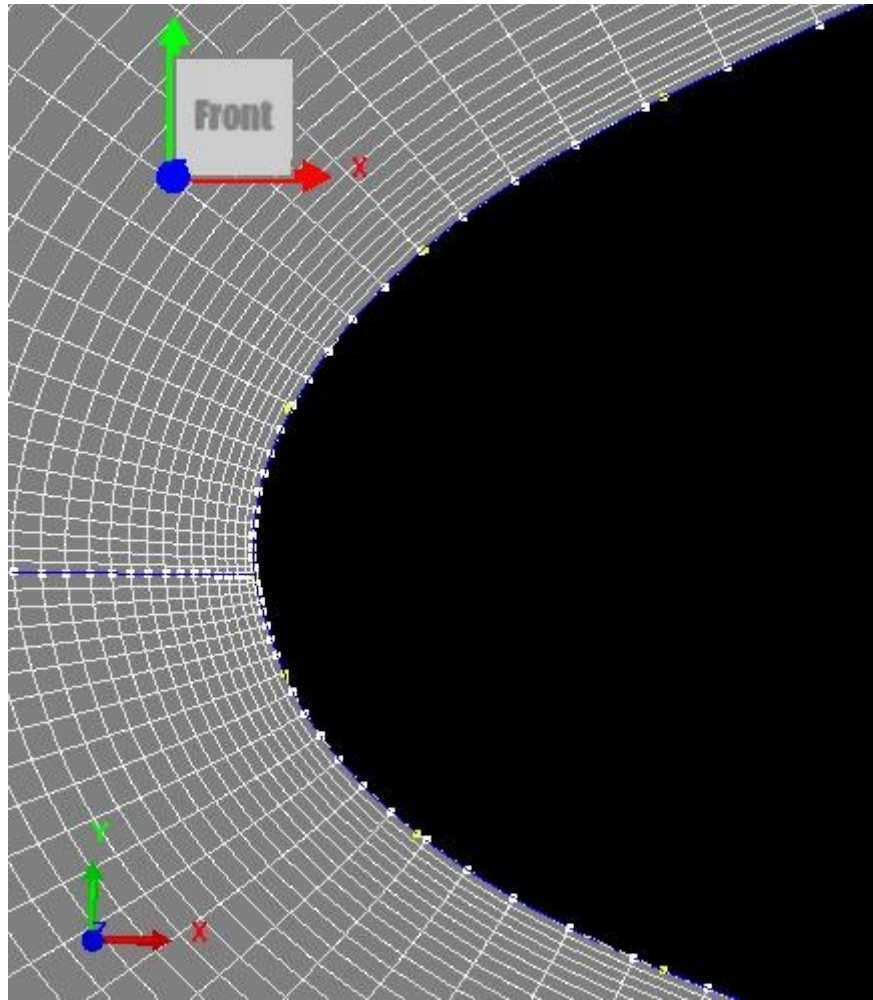


Figure 20. Leading edge close up

When the C-grid for the root chord section is complete, the same C-grid can be done on the tip chord of the wing. The outer bounds of the 3D mesh in the shape of an extruded C-grid was created 10 half-span lengths away from the wing as shown in figure 21. Notice that only a half of the wingspan is modeled and analyzed in CFD as it is a symmetrical wing, so the solution on the right wing can be duplicated on the left wing in the postprocessing step.

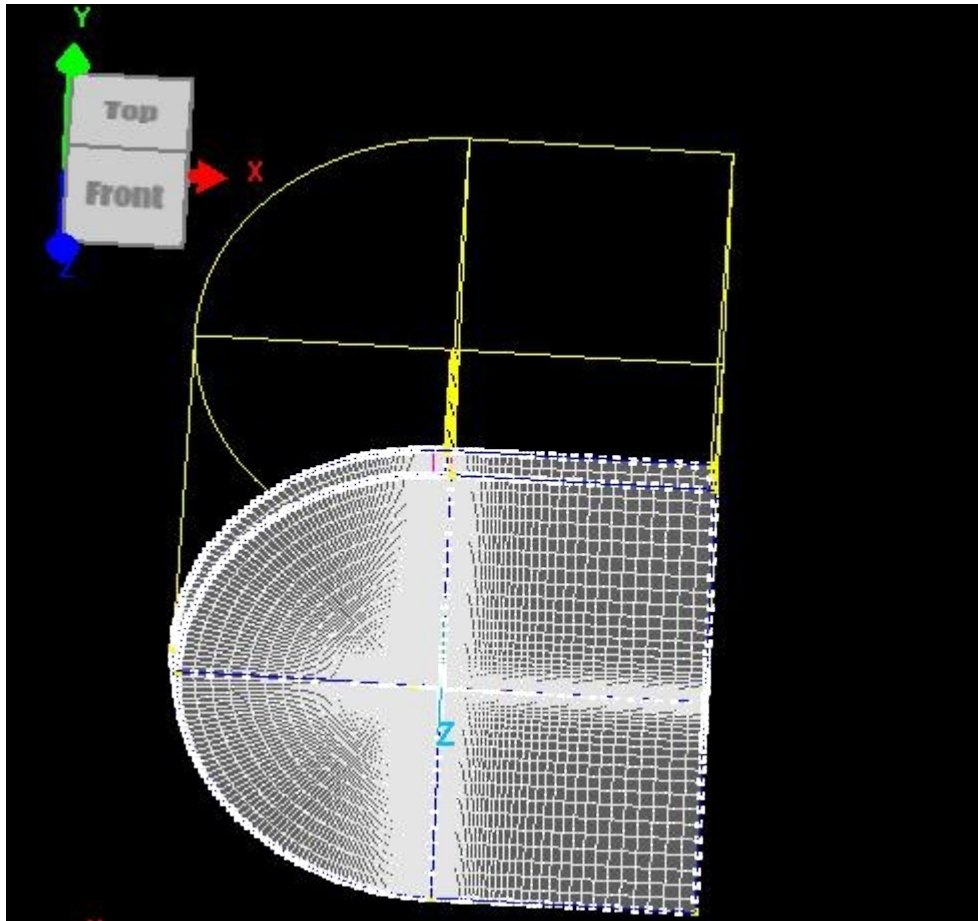


Figure 21. 3D mesh geometry setup

After placing edges on all of the exposed lines connecting the C-grids, the grid point spacings were adjusted to achieve higher resolution at the leading edge and the trailing edge, and to respect the y^+ value of 1. The minimum cell sizing for boundary layer solution was not only applied around the airfoil surfaces, but also at the wing tip as seen by the concentration of grid points in Figure 22.

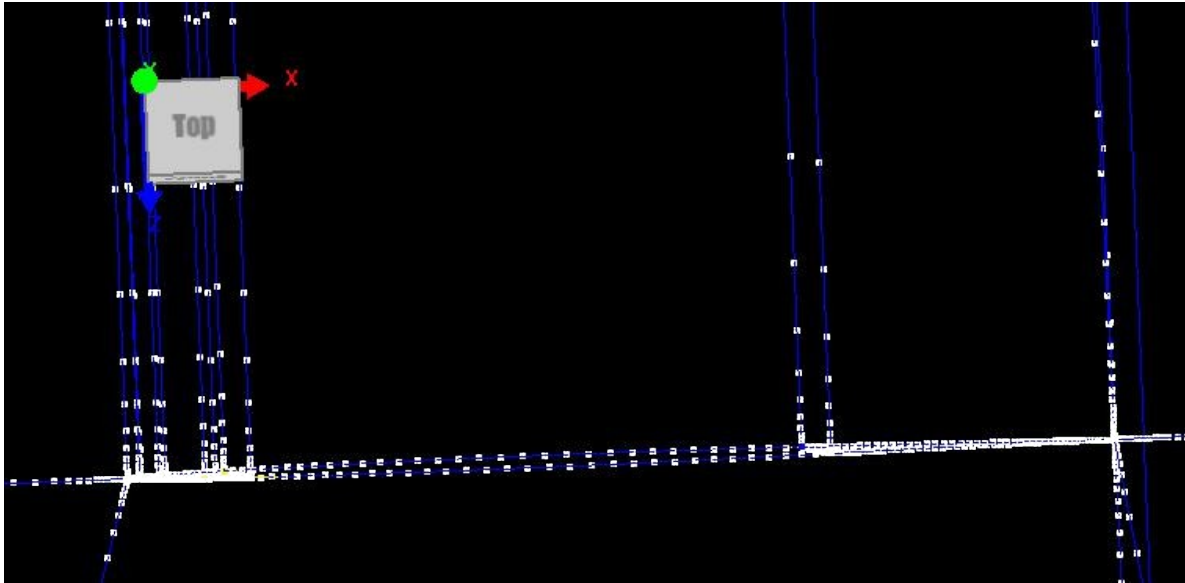


Figure 22. Wing-tip close up

One complication with structure meshing a 3-D wing is the representation of the wing-tip. As mentioned above, a face is defined by 4 sets of edges. However, a wing-tip profile only contains the airfoil's top surface and the bottom surface. In order to mesh the wing-tip geometry, the wing-tip profile was divided up into smaller faces as shown in Figure 23. The round leading edge was divided up using the butterfly function, and the trailing edge was represented by a face of only three edges, which results in a singularity point at the trailing edge.

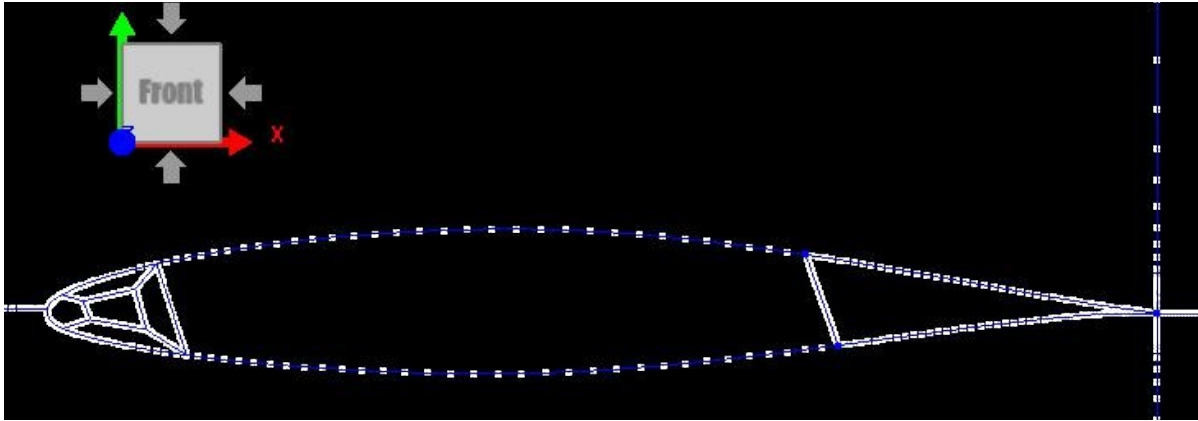


Figure 23. Wing tip mesh nodes

Next, all of the available faces were formed from the edges to represent the cell boundaries as illustrated in figure 24.

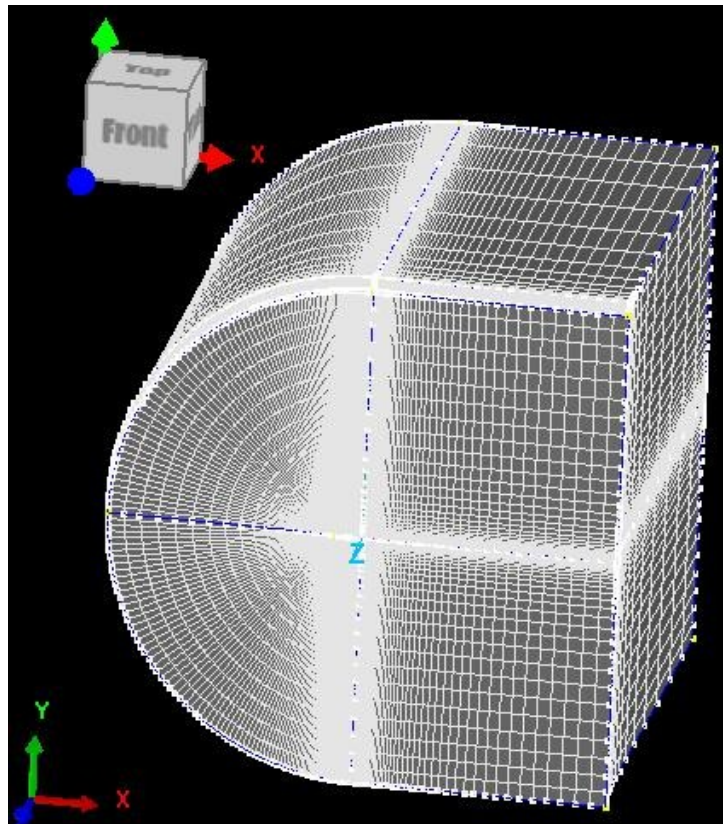


Figure 24. Structured mesh faces

Finally, individual volumetric cells were formed by making blocks from the above faces. Each block is created by selecting 6 sets of faces defining a closed volume. The created cells can be viewed using the Grid Viewer function as shown in figure 25. In the end, approximately 3.5 million cells are created from the method described above. After double checking the quality of the cells, the angle of attack of the wing was implemented by using the rotation tool in GEOM. The angle of attack corresponds to a lift coefficient of 0.47 and is obtained from the AVL parametric studies. Finally, the mesh was saved as .DTF and imported to a solver.

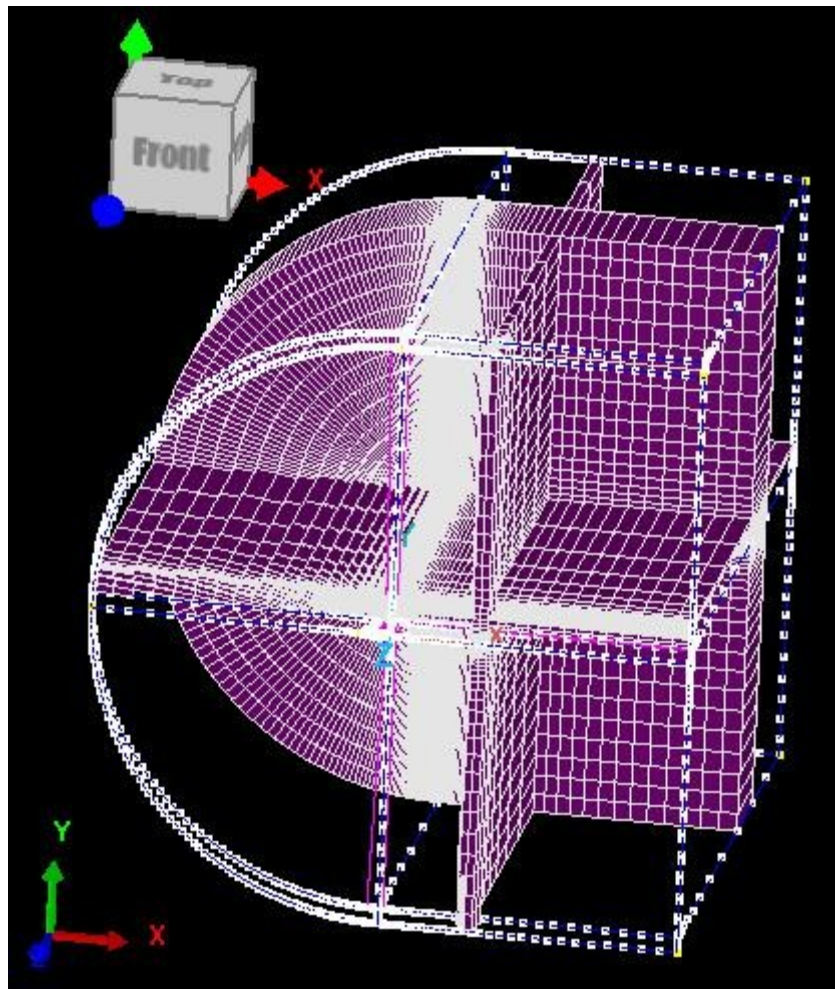


Figure 25. Cells in 3-D mesh

Setting up the mesh for the wing with a winglet was more challenging as the complicated geometry could easily result in cells with negative values which would be impossible to export to a solver. To mitigate this issue, several layers of C-grid were meshed from the wing surface, gradually expanding to a large C-grid as shown in figures 26 and 27. This process turned out to be much more time consuming and resulted in more blocks and cells.

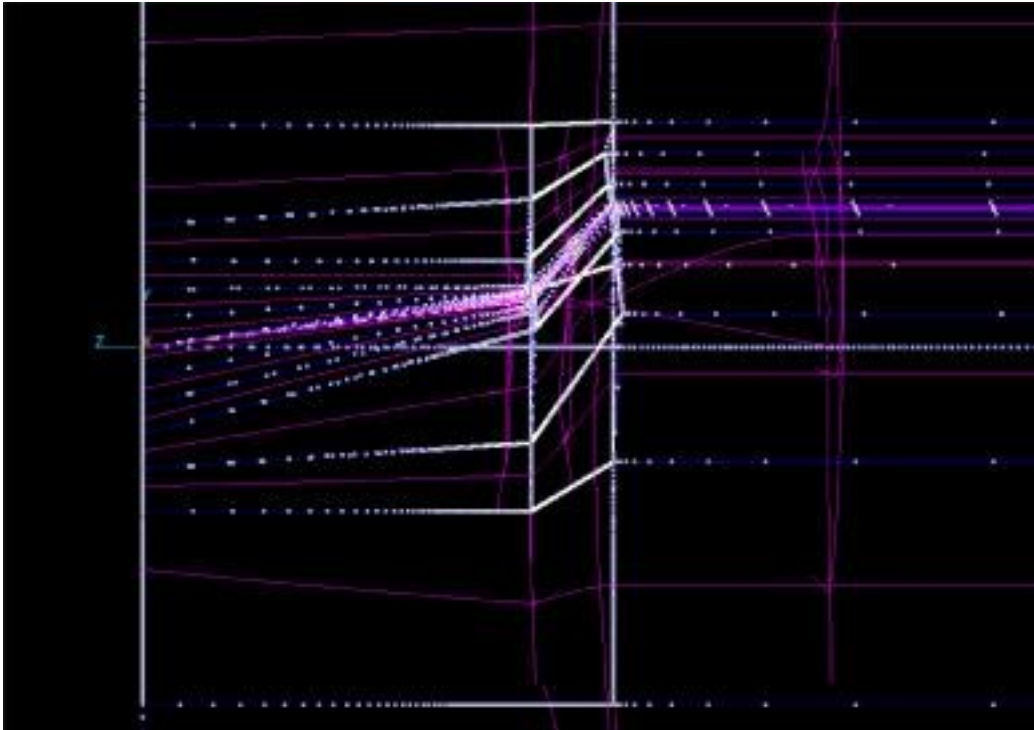


Figure 26. Internal view of layered mesh on the winglet

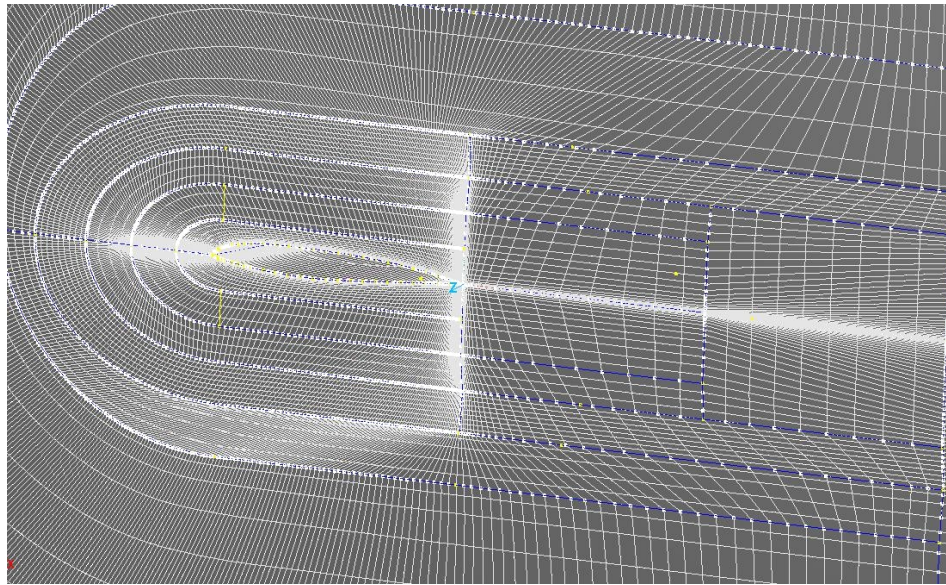


Figure 27. Layered C-grids on the wing with winglet

Solver Setup

An important part of solver setup is determining the flow model. FASTRAN contains three model options: inviscid, Navier-Stokes(Laminar), and Navier-Stokes(Turbulent). For low fidelity studies, inviscid solutions can be run to achieve a solution in a relatively short time. However, viscous effects need to be adequately captured in analyzing a winglet since there is significant boundary layer interaction at the joint between the wing and the winglet. The Reynolds number at aircraft cruise condition is high enough that the flow is best characterized as turbulent where the momentum of the fluid flow dominates the viscous effects. In order to achieve the most realistic solution, turbulent Navier-Stokes flow model simulations were desired.

When the flow is laminar, or uniform, the fluid flow can be characterized through solving the steady-state Navier-Stokes equation. With the introduction of turbulence, however, the problem becomes time-variant due to the chaotic mixing brought on by eddies. Consequently,

simulating turbulence is best achieved by estimating macroscopic flow characteristics by the means of averaging out the fluctuations and instantaneous fluid movements. This method of simulation is called Reynolds Averaged Navier-Stokes, or RANS.

One type of RANS is the k-ε model which was utilized in this study. k-ε model describes the turbulence using two partial differential transport equations shown in equations 9 and 10 (CFD-FASTRAN V2014.0 User Manual, 2014). Equation 9 is used to calculate the turbulent kinetic energy *k*, and equation 10 calculates the turbulent dissipation rate ε.

$$\frac{d}{dt} \int_V \rho k \, dV + \nabla_j \int_V \rho k v_j \, dV = \int_V \rho \left(\nu \nabla^2 k + G_k - \epsilon \right) dV$$

Equation 9

$$\frac{d}{dt} \int_V \rho \epsilon \, dV + \nabla_j \int_V \rho \epsilon v_j \, dV = \int_V \rho \left(\nu \nabla^2 \epsilon + C_{\epsilon 1} \frac{\epsilon}{k} G_k - C_{\epsilon 2} \frac{\epsilon^2}{k} \right) dV$$

Equation 10

While setting up FASTRAN, *k* and ε were both user-input parameters that had to be calculated based on the flow simulation. The turbulent kinetic energy, *k*, is calculated using equation 11, where *U* is the bulk velocity of the flow and the term *I* is the turbulent intensity, which is calculated with equation 12.

$$k = \frac{3}{2} U^2 I^2$$

Equation 11

Equation 12

It is important to note that equation 12 is considered for internal flows. For external flows, such as the wing simulation, the intensity value can be as low as 0.0005, and that was the value used in the solver setup. Turbulence dissipation rate, ϵ , is calculated with equation 13, where β is the ratio of turbulent to laminar viscosity and ranges from 0.1 to 1 for external flows (ESI-CFD Support Team, 2011).

$$\frac{\epsilon}{\rho} = \frac{1.92 C_{\mu}^{3/4} k^{3/2}}{\beta \rho}$$

Equation 13

Chapter 3 Results

AVL Parametric Study

Table 1 summarizes the results of AVL parametric study organized by airfoils. All three kinds of airfoils achieved at least 8 percent decrease in induced drag, but the most effective winglet airfoil turns out to be the Whitcomb airfoil with 11% decrease in induced drag. This makes sense as the rest of the winglet geometries were that of the Whitcomb winglet for which the Whitcomb airfoil was optimized.

Table 1: Airfoil Comparison of AVL results

| | Whitcomb | BAC | Sailplane |
|----------|----------|------|-----------|
| C_{di} | 0.89 | 0.92 | 0.91 |

Figure 28 illustrates a chart that plots the average induced drag of the winglet based on the winglet dihedral angle. Contrary to Whitcomb's report and agreeing with Ning's findings, the results slightly suggest the use of tip extension over a winglet with the best dihedral angle being around 30 degrees.

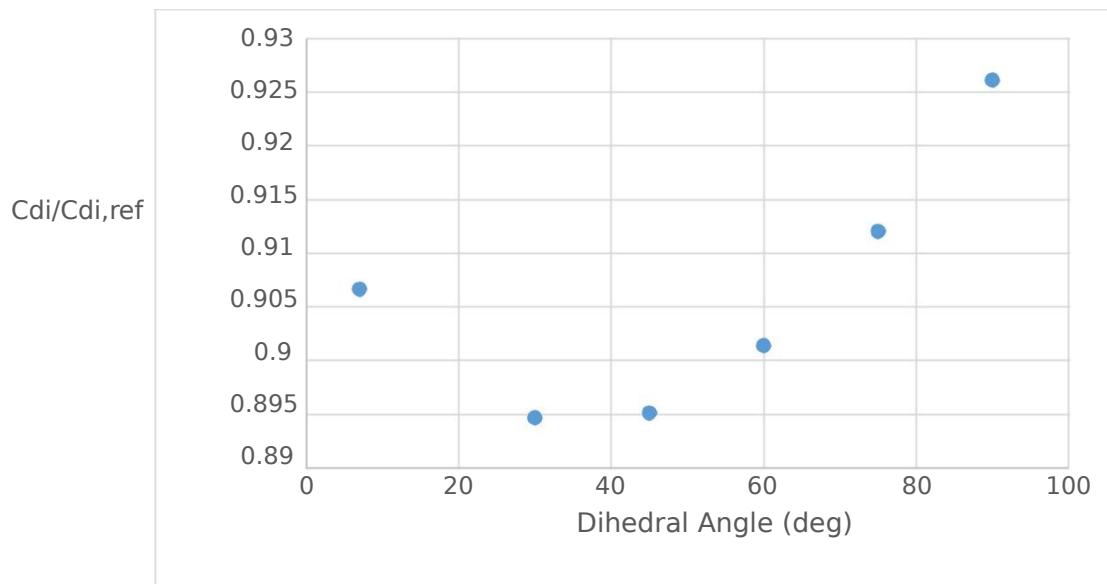


Figure 28. Winglet dihedral angle effect

The results of toe-out angle illustrated in figure 29 was a bit unexpected as the induced drag only got higher and higher the more the winglet was rotated. The unexpected finding, however, is a logical answer as only the induced drag is plotted here. As the toe-out angle of the winglet increases, more lift is generated by the winglet, and thus more lift induced drag is generated. The benefit of a forward-pointing lift force is not captured through vortex lattice method as the downwash angle at the Trefftz plane would pick up the increased induced drag and not the additional thrust.

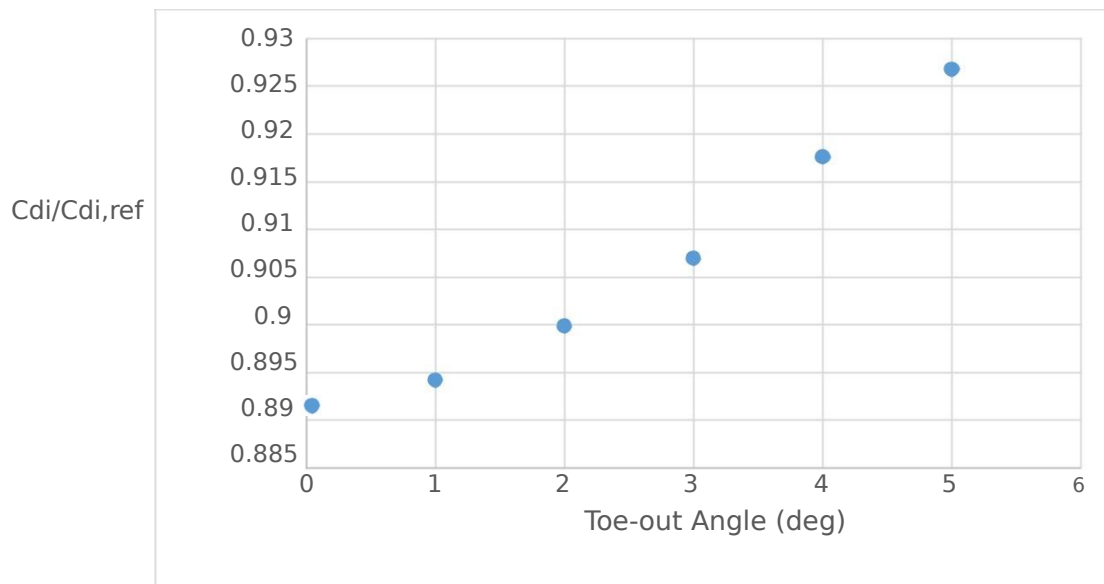


Figure 29. Winglet toe-out angle effect

From the low fidelity parametric study, the winglet that delivered the largest decrease in induced drag was found to be the Whitcomb airfoil winglet at 45° dihedral and 0° toe-out which resulted in 12.5% decrease in induced drag. Recalling that induced drag is about 40% of the total drag at cruise condition, 12.5% induced drag reduction is equated to about 5% decrease in the overall drag. The optimized winglet design developed through inviscid parametric study is in line with the Pareto front calculated in Ning’s study in figure 7.

The vortex lattice method utilized in AVL has several limitations that doesn’t allow the most realistic aerodynamic solutions to be obtained. Because the method is only valid for inviscid flow only, the calculation fails to capture the boundary layer interaction at the wing and winglet joint. Because the wing is modeled by manually inputting the chord location at different sections of the wing, it is difficult to model the curved surfaces and geometries of the wingtip design. Finally, wave drag is definitely a factor to be considered at Mach .85 cruising speed, but

compressibility is also omitted in vortex lattice method. Therefore, CFD analysis will be carried out for the base wing, the wing with the optimized winglet design, and the same wing plus winglet combo with a 2° winglet toe-out angle. CFD analysis will be able to capture the viscous, compressible flow while providing a more sophisticated means of modeling the 3D wing. Also, the winglet toe-out angle will be visited again to analyze its effectiveness in a more realistic simulation.

CFD Analysis

Despite setting the turbulence parameters with the values suggested by the ESI reference, turbulence modeling turned out to be a huge challenge as none of the simulations achieved residuals below the industry standard convergence criteria of 0.0001. Despite trying different turbulence parameters, the turbulence residuals would start the divergence trend, oscillate, and eventually interfere with the convergence of the rest of the residuals as shown in figure 30. Most of the time the turbulence residual would fully diverge and stop the simulation abruptly. Also, there were many cases where several cells within the simulation would reach negative density or temperature values, which also interfered with the simulation from converging to a solution.

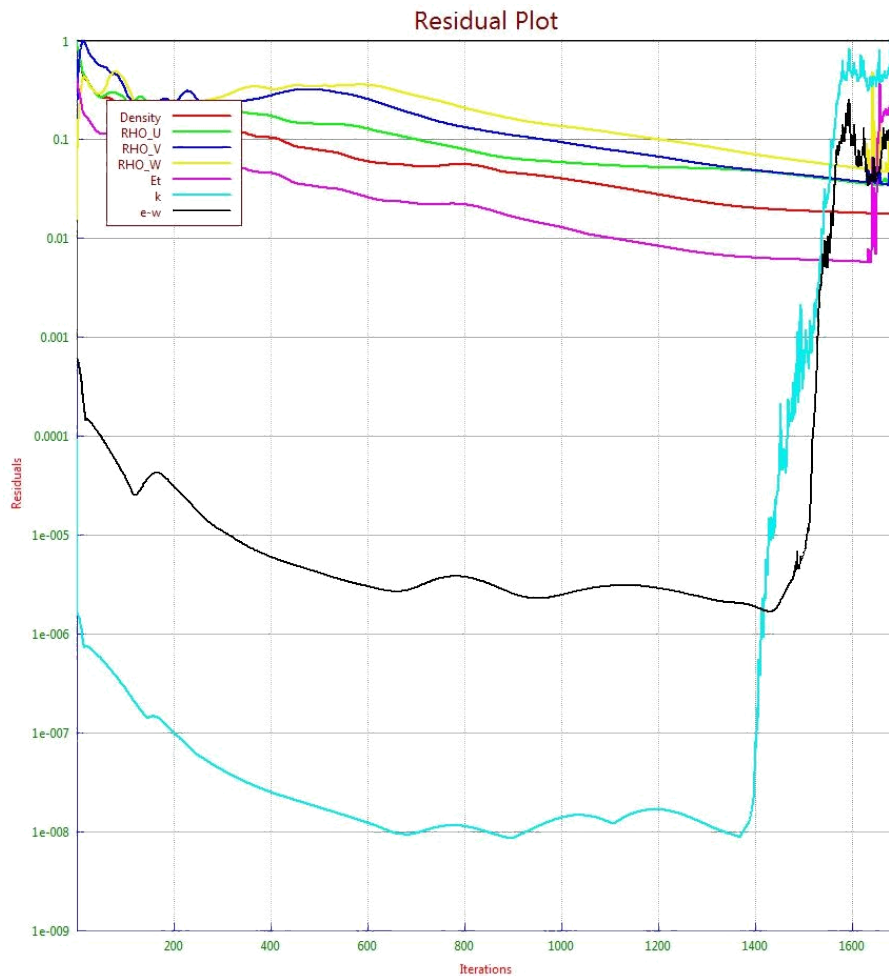


Figure 30. Unsuccessful turbulence simulation residual plot

In many cases where the residual plot couldn't be used to determine whether the simulation had converged to a solution, the force values from the output file was plotted against iterations to review the convergence history of the variable as illustrated in figure 31. When it was determined that obtaining a good answer with turbulence modeling was difficult with the allotted time for the study, laminar simulations were also executed in attempts to achieve more converged solutions.

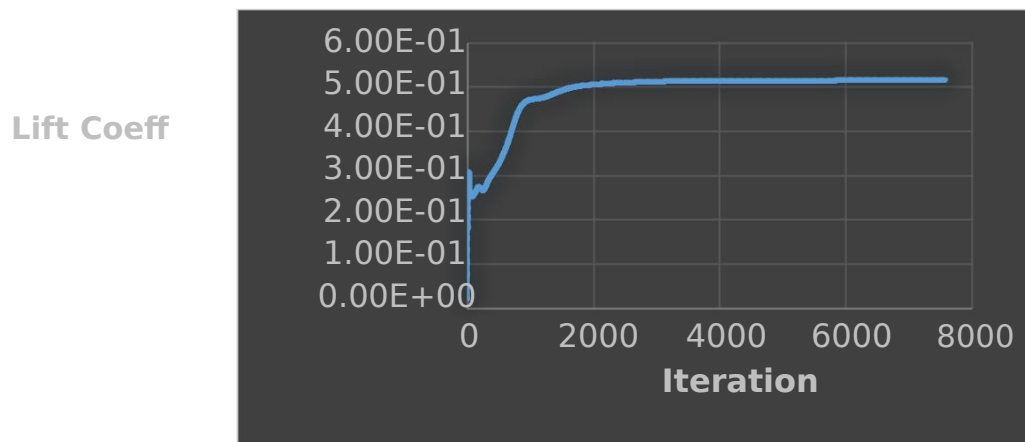


Figure 31. Convergence history monitoring.

Table 2 summarizes the CFD results. In an attempt to validate the CFD setup and results, the outputs of turbulent simulations of the base wing was compared to the aerodynamic coefficients of the actual Boeing 747 obtained from Roskam textbook (Part VI: Preliminary Calculations of Aerodynamic, Thrust and Power Characteristics, 2000). Even though the calculated lift coefficient is within 10% of the actual lift coefficient, the drag coefficient is higher than the real value by nearly 100%. The drag coefficient output was even higher for the wings with winglet, regardless of whether the simulation was turbulent or not. Because the drag coefficient is so high, the lift-drag ratio of the wings with winglet came out lower than that of the base wing. It was not possible to validate the optimized design as inviscid results and the CFD results did not agree with each other. One positive, and expected result was revealed when comparing a wing with the winglet to a wing with the winglet toe angle. The wing with a 2° toe-out winglet achieved about 4% less total drag than the wing with a 0° toe-out winglet. This finding physically makes sense and agrees with the literature as the forward component of the winglet lift can negate some of the drag on the wing.

Table 2 CFD results summary

| | C_L | C_D | C_L/C_D | D_{TOT} |
|---------------------|-------|--------|-----------|-----------|
| Real Wing | 0.47 | 0.03 | | |
| Base Wing | 0.426 | 0.0556 | 7.7 | |
| Winglet (Turbulent) | 0.49 | 0.0701 | 6.99 | |
| Winglet (Laminar) | 0.515 | 0.069 | 7.47 | 481400N |
| Toe-out (Laminar) | 0.511 | 0.068 | 7.52 | 474000N |

Despite not obtaining much useful force output from the simulations, CFD-VIEW was used to extract several contour plots that make physical sense. Figures 32 and 33 show the pressure contour plots at locations aft of the base wing's wingtip. In figure 32, the wingtip vortex is clearly represented by the circular region of low pressure directly behind the wingtip, and in figure 33, 3.5 m past the wingtip, the vortex seemingly dissipated as the circular region has gotten bigger, and the central low pressure has a higher pressure value. The existence of a wingtip vortex is further supported by figure 34 which illustrates a set of streamlines going past the wingtip region. As the streamlines are viewed from the direction of freestream flow, there clearly is circular motion to all of the streamlines as they seem to form concentric circles around the wingtip region.

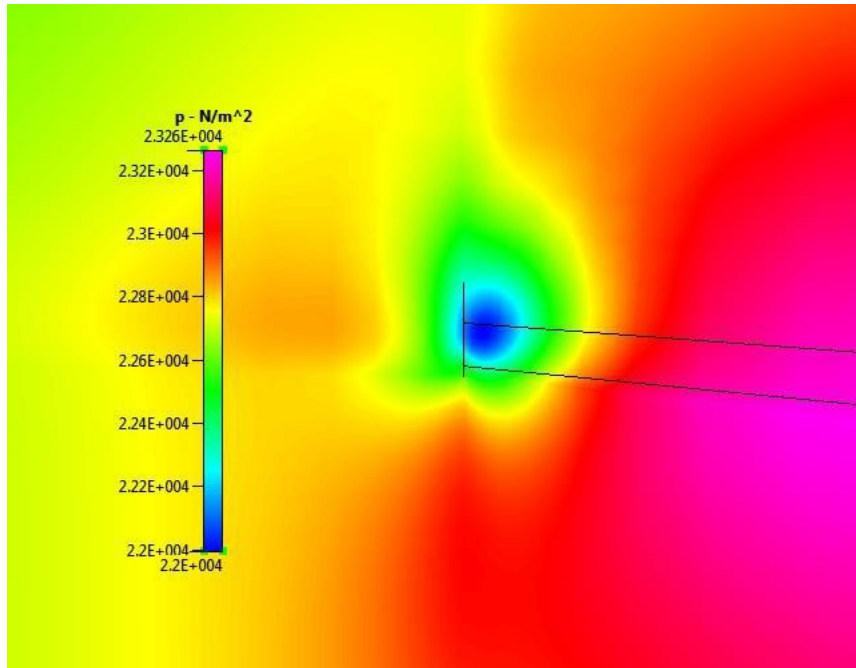


Figure 32. Pressure contour at 0.5 m past base wing

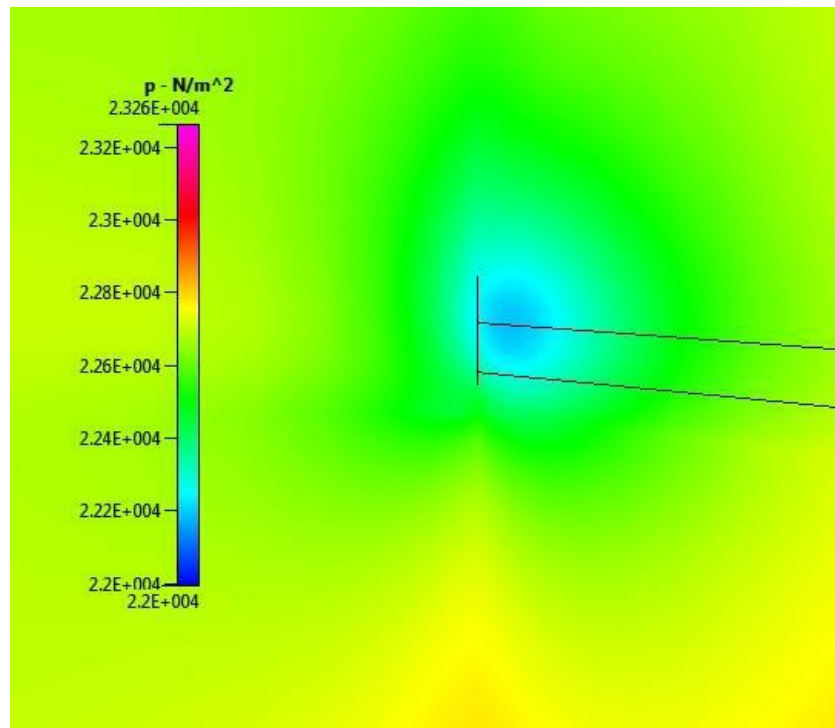


Figure 33. Pressure contour at 3.5m past base wing

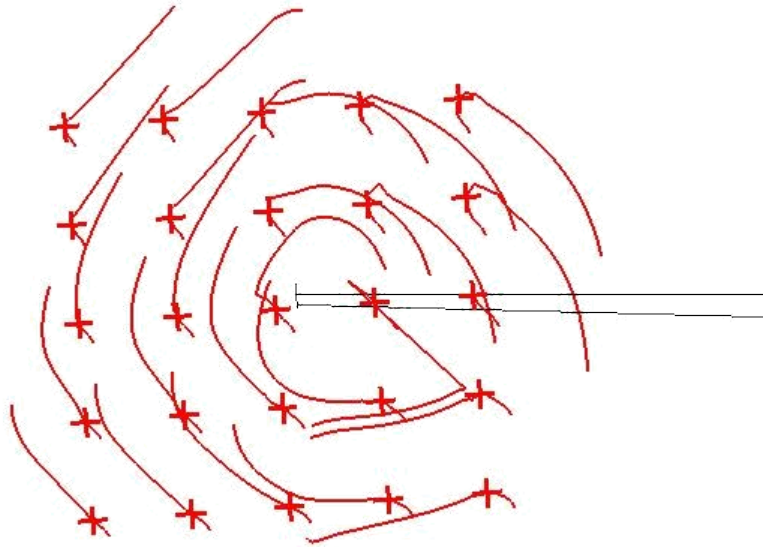


Figure 34. Streamlines past a base wing

Even though the simulation provided drag coefficient that did not agree with the actual data, the base wing achieved a well resolved boundary layer as seen by the y^+ values on the wing surface illustrated in figure 35. Most of the base wing's surface has a y^+ value of 1 or below.

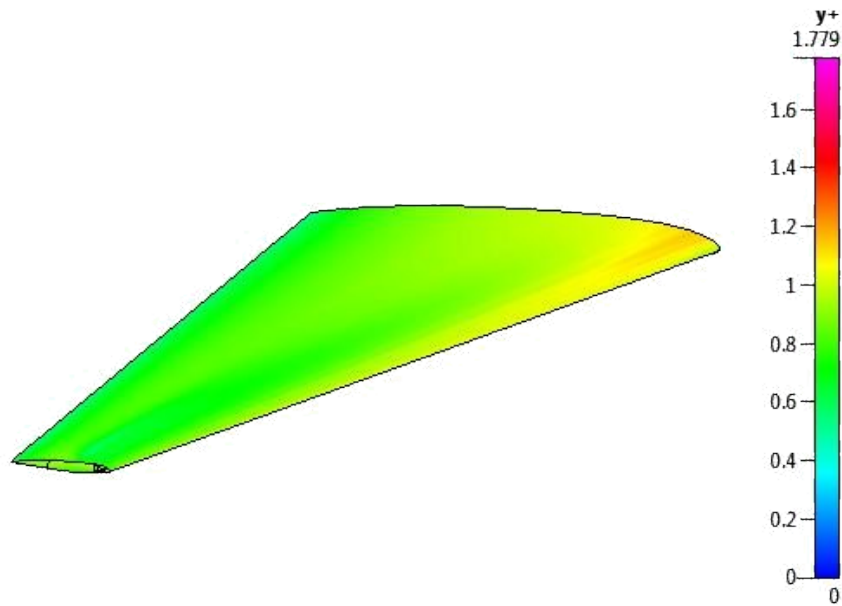


Figure 35. Y+ contour plot on base wing surface

There was even less success with the modeling the wing with winglet as diverging turbulence residuals caused the simulation to error out even before the aerodynamic forces had converged to a value. The convergence history in figure 36 shows that the lift coefficient of the turbulent winglet simulation hadn't settled on a value before the simulation stopped.

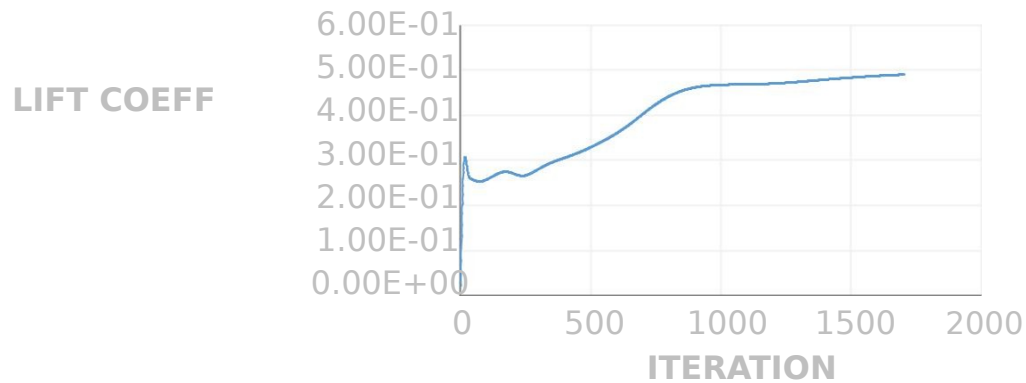


Figure 36. Convergence history of wing with winglet in turbulence

The signs of premature stopping of the simulation appeared in other plots as the y^+ contour plot in figure 37 reveals incomplete solution of the boundary layer with the y^+ values ranging up to 49. Also, there are signs of simulation error compounded by inadequate meshing in figures 38 and 39 where the pressure contour plots feature the shapes of the meshing around the wing or winglet geometry. It is both possible that the complicated layered C-grid meshing needs more iterations to resolve these areas or the meshing needs more improvement, so that the solver has an easier time converging to a solution.

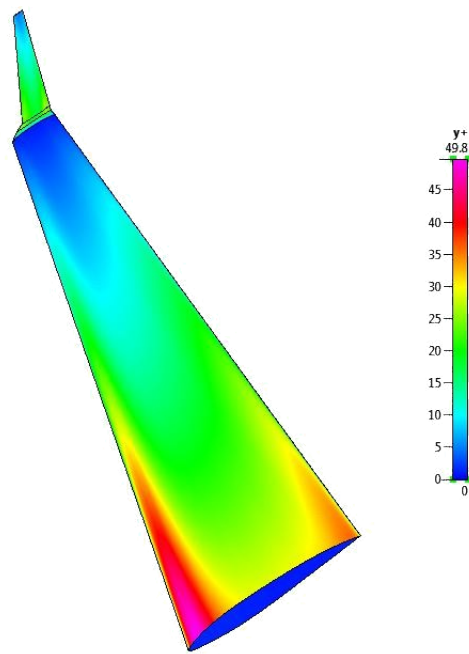


Figure 37. Y+ contour plot of winglet wing with turbulence

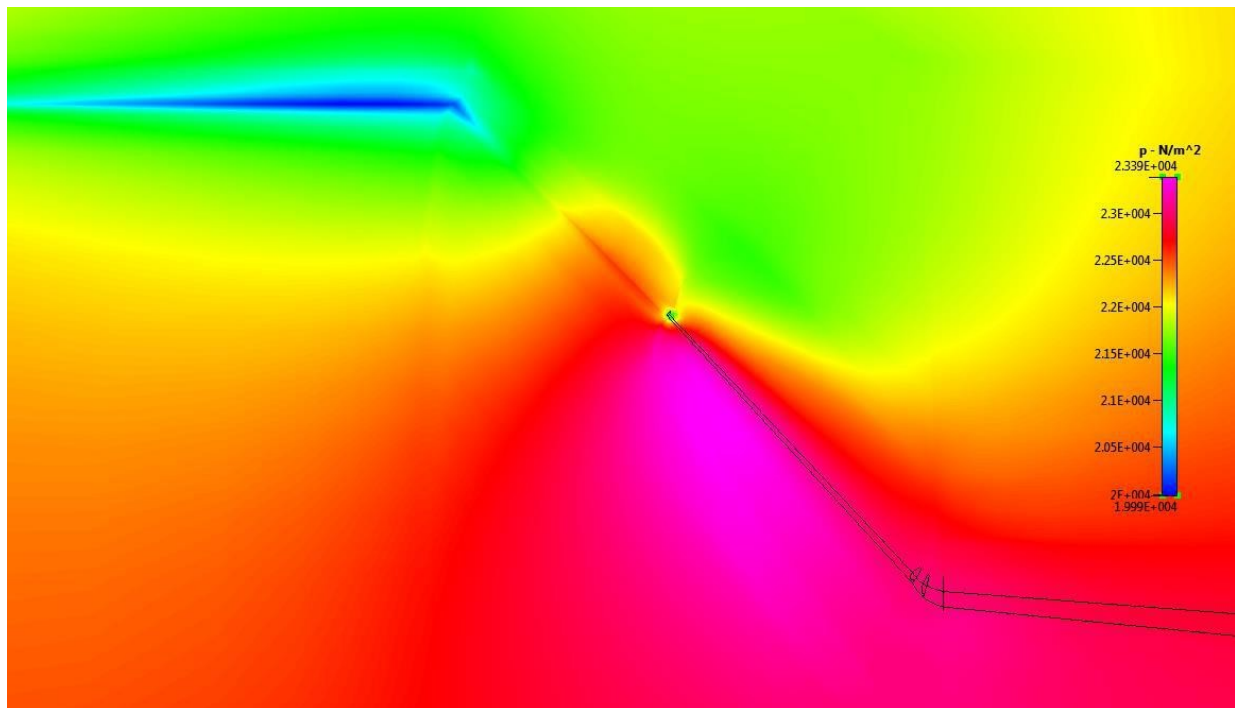


Figure 38. Pressure contour plot around the winglet with turbulence

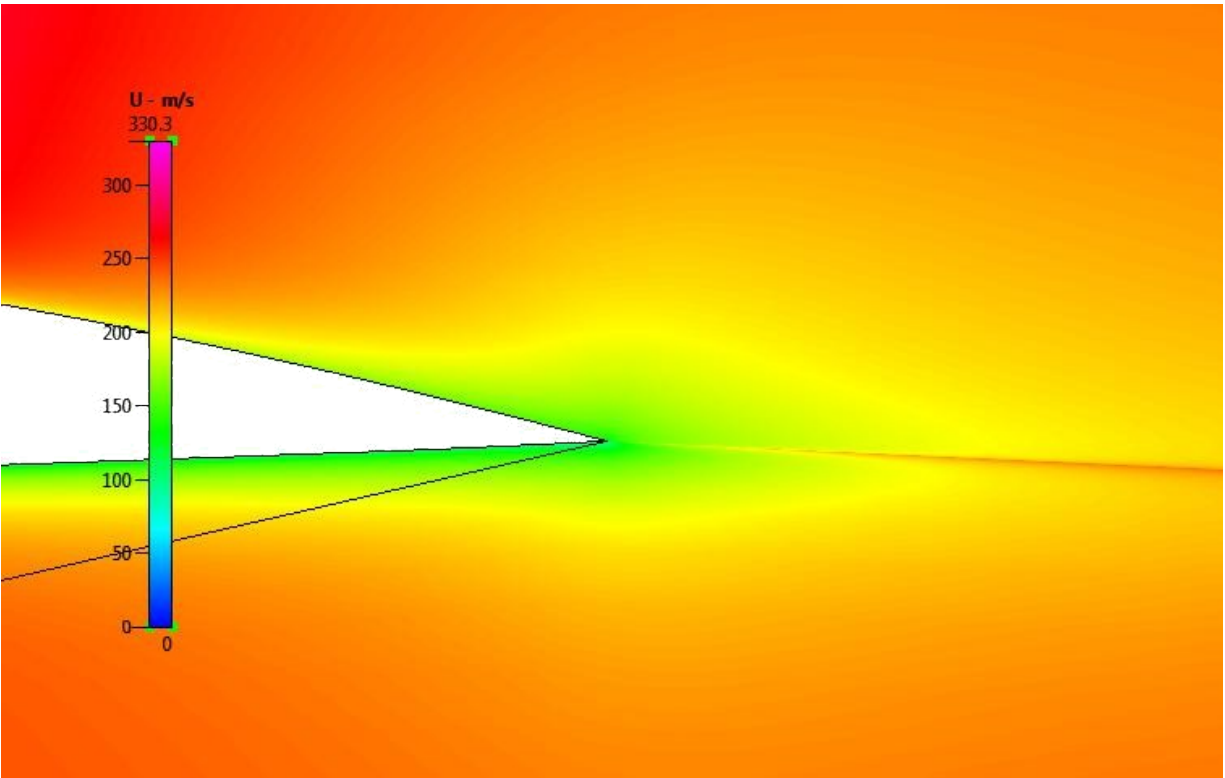


Figure 39. Pressure contour plot around the trailing edge of winglet wing with turbulence

The boundary layer solution for the winglet wing even failed to converge in laminar flow as illustrated by the high y^+ values observed in figure 40. In laminar flow, the boundary layer solution appears to be a bit more resolved than the turbulent simulation as the highest observed y^+ values is down to 29.

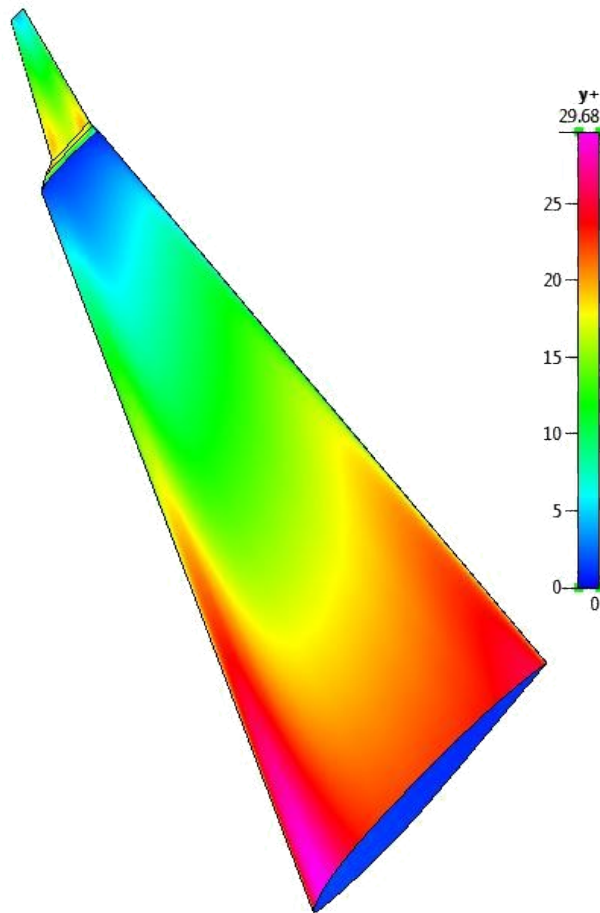


Figure 40. Y+ contour plot on the surface of winglet wing in laminar flow

Despite not delivering the aerodynamic forces that validate the effectiveness of the winglet, the qualitative plots in figures 41 and 42 still confirm the functionality of the winglet. The pressure contour plot right behind the winglet reveal that the vortex is not being formed at the tip of the winglet, and not at the tip of the base wing. Moving the vortex generation away from the main wing increases efficiency of the wing by increasing the lift generation due to there being less vortex interference at the wingtip.

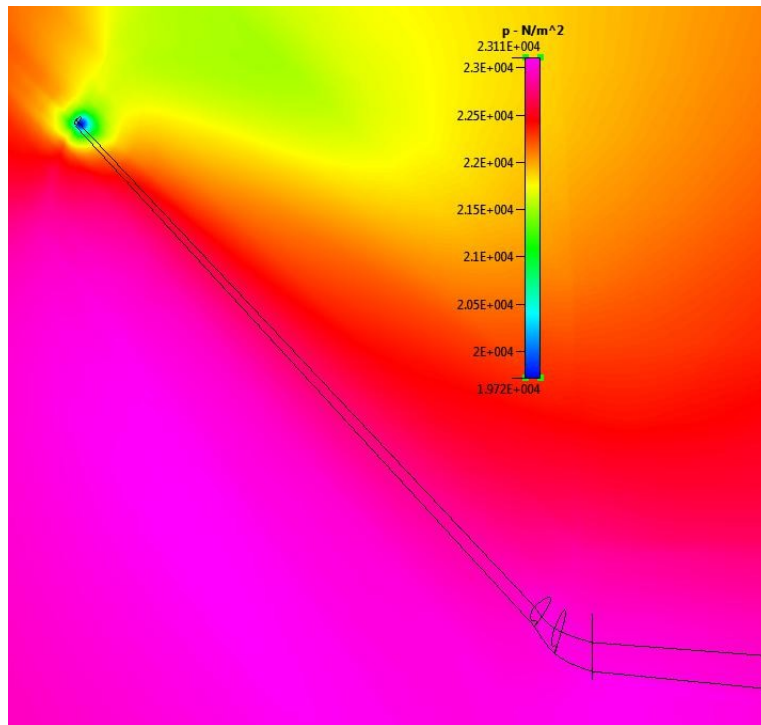


Figure 41. Pressure contour plot 0.5m behind winglet in laminar flow

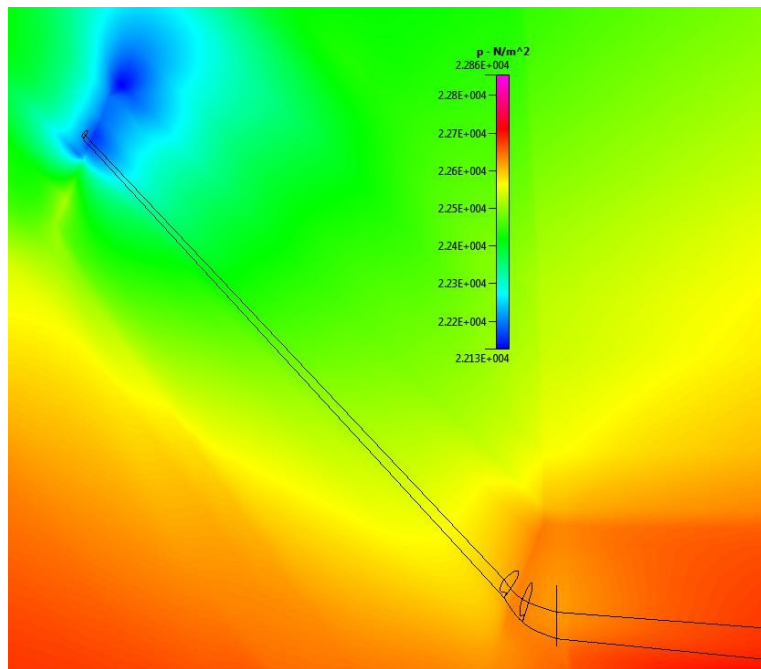


Figure 42. Pressure contour plot 3.5m behind winglet in laminar flow

Chapter 4 Conclusion

Using vortex lattice method, winglet to retrofit a Boeing 747-100 wing was optimized to reduce induced drag by 12.5%. The aerodynamic load output from the CFD simulations did not agree with the inviscid analysis of the winglet design, but the qualitative plots achieved from CFD explained some physics behind a flow past a winglet. More literature review of the turbulence modeling and meshing is needed before a good solution from computational fluid dynamics can be achieved. Correct turbulence parameter must be calculated with a better understanding of the physics behind the simulation. More time needs to be spend on the mesh to avoid any grid dependencies. Finally, numerical methods merely provide direction for optimization and are not the definitive answer. For any numerical optimization, wind-tunnel testing is necessary for obtain validation of the design.

References

- Airbus. (2009, 11 15). *Airbus launches "Sharklet" large wingtip devices for A320 Family with commitment from Air New Zealand*. Retrieved 6 21, 2014, from Airbus: <http://www.airbus.com/presscentre/pressreleases/press-release-detail/detail/airbus-launches-sharklet-large-wingtip-devices-for-a320-family-with-commitment-from-air-new-zealan/>
- Allward, M. (1989). Wingtip Technology. In J. Motum, *Putnam Aeronautical Review* (Vol. 1, p. 41). London: Conway Maritime Press Ltd.
- Bargsten, C. (2011). Winglets: Striving for Wingtip Efficiency. In B. Clayton, & M. Gibson, *NASA Innovation in Aeronautics: Select Technologies That Have Shaped Modern Aviation* (pp. 11-12). Washington, DC: NASA.
- Boeing. (2015). *Boeing 747*. Retrieved from Boeing: <http://www.boeing.com/commercial/747/>
- BOEING BACXXX AIRFOIL (bacxxx-il)*. (2015). Retrieved from Airfoil Tools: <http://airfoiltools.com/airfoil/details?airfoil=bacxxx-il>
- Bourdin, P., Gatto, A., & Friswell, M. (2007). Potential of Articulated Split Wingtips for Morphing-Based Control of a Flying Wing. *25th AIAA Applied Aerodynamics Conference* (p. 1). Miami: AIAA.
- Céron-Muñoz, H. D., Cosin, R., & Coimbra, R. (2013, 3). Experimental Investigation of Wing-Tip Devices on the Reduction of Induced Drag. *Journal of Aircraft*, *50*(2), 441-449.
- CFD-FASTLAN V2014.0 User Manual. (2014, July). Huntsville, Alabama: ESI CFD.

Compute Grid Spacing for a Given Y+. (2015, May 14). Retrieved from PointWise:

<http://www.pointwise.com/yplus/>

ESI-CFD Support Team. (2011, 8 31). *How to estimate turbulence quantities to specify at inlet*

boundaries. Retrieved from ESI CFD FAQ: [http://www.esi-cfd.com/faq/index.php?](http://www.esi-cfd.com/faq/index.php?action=artikel&cat=4&id=156&artlang=en)

[action=artikel&cat=4&id=156&artlang=en](http://www.esi-cfd.com/faq/index.php?action=artikel&cat=4&id=156&artlang=en)

Faye, R., Laprete, R., & Winter, M. (2002, 1 1). Blended Winglets. *Aero*(17), pp. 16-31.

Kinney, J. (2010). *NASA's Contribution to Aeronautics : Aerodynamics, Structures, Propulsion, and Controls* (Vol. 1). (R. Hallion, Ed.) Washington, DC: NASA.

Liepmann, H. W., Rothko, A., & Lindsay, R. B. (1957). Physics Today. In *Elements of Gasdynamics*. John Wiley & Sons, Inc.

Ning, S. A., & Kroo, I. (2010, 3). Multidisciplinary Considerations in the Design of Wings and Wing Tip Devices. *Journal of Aircraft*, 47(2), 534-543.

Part VI: Preliminary Calculations of Aerodynamic, Thrust and Power Characteristics. (2000). In J. Roskam, *Airplane Design* (p. 114). DARcorporation.

Shafer, D., Pemridge, J., & reilly, M. (2004). Winglets. Virginia Tech University.

Wald, M. L., & Baker, A. (2001, 11 19). A Workhorse of the Skies, Perhaps With a Deadly Defect. *The New York Times*.

Weierman, J., & Jacob, J. D. (2010). Winglet Design and Optimization for UAVs Jacob. *28th AIAA Applied Aerodynamics Conference* (p. 3). Chicago: AIAA.

Whitcomb, R. T. (1976). *A Design Approach and Selected Wind-tunnel Results at High Subsonic Speeds for Wing-tip Mounted Winglets*. Washington, DC: NASA.

Yoon, J. (2003, 11 2). *Boeing 767 Raked Wingtips*. Retrieved 12 6, 2013, from Aerospaceweb:
<http://www.aerospaceweb.org/question/aerodynamics/q0148.shtml>

Zhang, H. J., Zhou, Y., & Whitelaw, J. H. (2006, 3). Near-Field Wing-Tip Vortices and Exponential Vortex Solution. *Journal of Aircraft*, 43(2), 445-449.

Appendix

Modeled B747-100 Wing Geometry

| | |
|---------------|--------------------|
| Span | 59.64 m |
| Area | 615 m ² |
| Root Chord | 16.56 m |
| Tip Chord | 4.06 m |
| Ref Chord | 11.5729 m |
| Quarter Sweep | 37° |
| Dihedral | 7° |

Simulation Parameters at Steady Cruise

| | |
|-------------------------------------|----------|
| U (m/s) | 248.1 |
| Mass (kg) | 227527 |
| Alt (m) | 11000 |
| P (kg/m ³) | 0.363918 |
| μ (m ² /s) | 1.43E-05 |
| P (Pa) | 22632.1 |
| T (K) | 216.65 |
| Cl | 0.47 |
| K (m ² /s ²) | 0.0231 |
| ϵ (J/kg-s) | 2.437 |

Airfoil Coordinates

| BACXXX | | Whitcomb Winglet | | PSU-90-125WL | |
|--------|--------|------------------|--------|--------------|---------|
| 1 | 0.0004 | 1 | -0.002 | 1 | 0 |
| 0.95 | 0.0116 | 0.975 | 0.0038 | 0.99646 | 0.00062 |
| 0.9 | 0.0218 | 0.95 | 0.0089 | 0.98627 | 0.00269 |
| 0.85 | 0.0307 | 0.925 | 0.0138 | 0.97034 | 0.0063 |
| 0.8 | 0.0384 | 0.9 | 0.0184 | 0.94931 | 0.01099 |
| 0.75 | 0.045 | 0.875 | 0.0228 | 0.92336 | 0.01635 |
| 0.7 | 0.0503 | 0.85 | 0.027 | 0.892 | 0.02238 |

| | | | | | |
|------|--------|-------|--------|-------------|---------|
| | | | | 65 | |
| 0.65 | 0.0548 | 0.825 | 0.0311 | 0.857 7 | 0.02912 |
| 0.6 | 0.0585 | 0.8 | 0.0349 | 0.819 08 | 0.03646 |

| | | | | | |
|--------|---------|--------|---------|---------|----------|
| 0.55 | 0.0613 | 0.775 | 0.0384 | 0.77741 | 0.04423 |
| 0.5 | 0.0636 | 0.75 | 0.0419 | 0.73333 | 0.05217 |
| 0.45 | 0.0654 | 0.725 | 0.0451 | 0.68748 | 0.05999 |
| 0.4 | 0.0667 | 0.7 | 0.0481 | 0.64048 | 0.06725 |
| 0.35 | 0.0673 | 0.675 | 0.0508 | 0.59265 | 0.07341 |
| 0.3 | 0.0674 | 0.65 | 0.0533 | 0.54409 | 0.07826 |
| 0.25 | 0.0665 | 0.625 | 0.0554 | 0.49509 | 0.08194 |
| 0.2 | 0.0643 | 0.6 | 0.0572 | 0.44618 | 0.08446 |
| 0.15 | 0.0599 | 0.575 | 0.0587 | 0.39787 | 0.0858 |
| 0.125 | 0.0566 | 0.55 | 0.0599 | 0.35064 | 0.08593 |
| 0.1 | 0.0521 | 0.5 | 0.0618 | 0.30495 | 0.08482 |
| 0.075 | 0.0465 | 0.45 | 0.0627 | 0.26123 | 0.08249 |
| 0.05 | 0.0384 | 0.4 | 0.0628 | 0.21989 | 0.07893 |
| 0.0375 | 0.0334 | 0.35 | 0.0621 | 0.18131 | 0.0742 |
| 0.025 | 0.0271 | 0.3 | 0.0605 | 0.14582 | 0.06835 |
| 0.02 | 0.0242 | 0.25 | 0.0581 | 0.11371 | 0.06149 |
| 0.015 | 0.0207 | 0.2 | 0.0547 | 0.08524 | 0.05373 |
| 0.005 | 0.0112 | 0.175 | 0.0525 | 0.06062 | 0.04523 |
| 0.0025 | 0.0078 | 0.15 | 0.0499 | 0.04002 | 0.03617 |
| 0.001 | 0.005 | 0.125 | 0.0469 | 0.02356 | 0.02681 |
| 0.0005 | 0.0037 | 0.1 | 0.0433 | 0.01134 | 0.01745 |
| 0 | 0 | 0.075 | 0.0389 | 0.00343 | 0.0085 |
| 0.0005 | -0.0018 | 0.05 | 0.0333 | 0.00002 | 0.00063 |
| 0.001 | -0.0027 | 0.0375 | 0.0296 | 0.0024 | -0.0059 |
| 0.0025 | -0.0043 | 0.025 | 0.0249 | 0.01088 | -0.01194 |
| 0.005 | -0.0058 | 0.0125 | 0.0179 | 0.02456 | -0.01782 |
| 0.015 | -0.0098 | 0.005 | 0.0119 | 0.04321 | -0.02324 |
| 0.02 | -0.0112 | 0.002 | 0.0077 | 0.06663 | -0.02804 |
| 0.025 | -0.0125 | 0 | 0 | 0.09462 | -0.03211 |
| 0.0375 | -0.0152 | 0.002 | -0.0032 | 0.12693 | -0.03539 |
| 0.05 | -0.0175 | 0.005 | -0.0041 | 0.16327 | -0.03786 |
| 0.075 | -0.0216 | 0.0125 | -0.006 | 0.20328 | -0.03951 |
| 0.1 | -0.0254 | 0.025 | -0.0077 | 0.24657 | -0.04033 |
| 0.125 | -0.0288 | 0.0375 | -0.009 | 0.29269 | -0.04037 |
| 0.15 | -0.032 | 0.05 | -0.01 | 0.34116 | -0.03965 |
| 0.2 | -0.0375 | 0.075 | -0.0118 | 0.39144 | -0.03822 |
| 0.25 | -0.0417 | 0.1 | -0.0132 | 0.443 | -0.0361 |
| 0.3 | -0.0445 | 0.125 | -0.0144 | 0.49525 | -0.03331 |
| 0.35 | -0.0458 | 0.15 | -0.0154 | 0.5477 | -0.02975 |

| | | | | | |
|------|---------|-------|---------|---------|----------|
| 0.4 | -0.0457 | 0.175 | -0.0161 | 0.60004 | -0.02548 |
| 0.45 | -0.0443 | 0.2 | -0.0167 | 0.65193 | -0.02083 |
| 0.5 | -0.0417 | 0.25 | -0.0175 | 0.70276 | -0.01622 |
| 0.55 | -0.0383 | 0.3 | -0.0176 | 0.75178 | -0.01192 |
| 0.6 | -0.0344 | 0.35 | -0.0174 | 0.79827 | -0.00814 |
| 0.65 | -0.0303 | 0.4 | -0.0168 | 0.84149 | -0.00502 |
| 0.7 | -0.026 | 0.45 | -0.0158 | 0.88073 | -0.00261 |
| 0.75 | -0.0218 | 0.5 | -0.0144 | 0.91534 | -0.00093 |
| 0.8 | -0.0174 | 0.55 | -0.0122 | 0.94469 | 0.00007 |
| 0.85 | -0.0132 | 0.575 | -0.0106 | 0.96829 | 0.00051 |
| 0.9 | -0.009 | 0.6 | -0.009 | 0.98567 | 0.00049 |
| 0.95 | -0.0047 | 0.625 | -0.0071 | 0.99638 | 0.00018 |
| 1 | -0.0004 | 0.65 | -0.0052 | 1 | 0 |
| | | 0.675 | -0.0033 | | |
| | | 0.7 | -0.0015 | | |
| | | 0.725 | 0.0004 | | |
| | | 0.75 | 0.002 | | |
| | | 0.775 | 0.0036 | | |
| | | 0.8 | 0.0049 | | |
| | | 0.825 | 0.006 | | |
| | | 0.85 | 0.0065 | | |
| | | 0.875 | 0.0064 | | |
| | | 0.9 | 0.0059 | | |
| | | 0.925 | 0.0045 | | |
| | | 0.95 | 0.0021 | | |
| | | 0.975 | -0.0013 | | |
| | | 1 | -0.0067 | | |

Winglet design configurations based on varying dihedral angle

| Dihedral Angle (deg) | 0 | 15 | 30 | 45 | 60 | 83 |
|---|----------|----------|---------|----------|---------|----------|
| Wingtip Span (m) | 6.2622 | 5.884959 | 5.50771 | 5.130477 | 4.75323 | 4.1748 |
| Total Wing Span (m) | 59.64 | 62.68628 | 65.1477 | 66.89559 | 67.8728 | 67.92736 |
| Wingtip Area (m ²) | 7.288366 | 7.288366 | 7.28836 | 7.288366 | 7.28836 | 7.288366 |
| Total Effective Wing Area (m ²) | 615 | 617.6343 | 620.268 | 622.903 | 625.537 | 629.5767 |
| Wing Ref Chord (m) | 11.5729 | 11.3749 | 11.2557 | 11.1922 | 11.1669 | 11.18 |

AVL Input File of B747-100

```

747-100
#Mach
 0.84
#IYsym  IZsym  Zsym
 0      0      0.0
#Sref   Cref   Bref
615.0   11.57  59.64
#Xref   Yref   Zref
0.25    0.0    0.0
#
#
#=====
SURFACE
Wing
#Nchordwise  Cspace  Nspanwise  Sspace
10           1.0    20         1.0
#
YDUPLICATE
0.0
#
ANGLE
0.0
-----
SECTION
#Xle   Yle   Zle   Chord  Ainc  Nspanwise  Sspace
0.     0.     0.    16.56  0.0   0          0
AFILE
boeing.dat
-----
SECTION
#Xle   Yle   Zle   Chord  Ainc  Nspanwise  Sspace
25.6   29.82  3.66  4.06   0.0   0          0
AFILE
boeing.dat

```

AVL Parametric Analysis Result

| Whitcomb | Toe-out Angle (deg) | | | | | | | | | | | |
|----------------|---------------------|------|--------|------|--------|------|--------|------|--------|------|--------|------|
| | 0 | | -1 | | -2 | | -3 | | -4 | | -5 | |
| Dihedral (deg) | Cdi | AoA | Cdi | AoA | Cdi | AoA | Cdi | AoA | Cdi | AoA | Cdi | AoA |
| 0 | 0.0111 | 3.22 | 0.0111 | 3.22 | 0.0111 | 3.22 | 0.0111 | 3.23 | 0.0112 | 3.23 | 0.0113 | 3.23 |
| 15 | 0.0109 | 3.16 | 0.0109 | 3.17 | 0.0109 | 3.18 | 0.0110 | 3.19 | 0.0111 | 3.20 | 0.0112 | 3.21 |

| | | | | | | | | | | | | |
|----|--------|------|--------|------|--------|------|--------|------|--------|------|--------|------|
| 30 | 0.0108 | 3.12 | 0.0108 | 3.14 | 0.0108 | 3.15 | 0.0109 | 3.17 | 0.0109 | 3.18 | 0.0110 | 3.20 |
| 45 | 0.0107 | 3.10 | 0.0107 | 3.12 | 0.0107 | 3.13 | 0.0108 | 3.15 | 0.0108 | 3.17 | 0.0109 | 3.19 |
| 60 | 0.0107 | 3.09 | 0.0107 | 3.11 | 0.0108 | 3.13 | 0.0108 | 3.15 | 0.0108 | 3.17 | 0.0109 | 3.19 |
| 83 | 0.0109 | 3.13 | 0.0109 | 3.15 | 0.0109 | 3.17 | 0.0109 | 3.18 | 0.0111 | 3.22 | 0.0111 | 3.22 |

| BACXX X | Toe-out Angle (deg) | | | | | | | | | | | |
|-------------------|---------------------|------|--------|------|--------|------|--------|------|--------|------|--------|------|
| | 0 | | -1 | | -2 | | -3 | | -4 | | -5 | |
| Dihedral (deg) | Cdi | AoA | Cdi | AoA | Cdi | AoA | Cdi | AoA | Cdi | AoA | Cdi | AoA |
| 0 | 0.0112 | 3.22 | 0.0113 | 3.23 | 0.0114 | 3.23 | 0.0116 | 3.23 | 0.0117 | 3.24 | 0.0119 | 3.24 |
| 15 | 0.0110 | 3.19 | 0.0111 | 3.20 | 0.0112 | 3.21 | 0.0114 | 3.23 | 0.0115 | 3.24 | 0.0117 | 3.25 |
| 30 | 0.0109 | 3.17 | 0.0110 | 3.19 | 0.0111 | 3.20 | 0.0112 | 3.22 | 0.0114 | 3.21 | 0.0116 | 3.26 |
| 45 | 0.0108 | 3.16 | 0.0109 | 3.18 | 0.0110 | 3.19 | 0.0112 | 3.21 | 0.0113 | 3.23 | 0.0115 | 3.25 |
| 60 | 0.0109 | 3.16 | 0.0109 | 3.18 | 0.0110 | 3.20 | 0.0111 | 3.22 | 0.0113 | 3.23 | 0.0114 | 3.25 |
| 83 | 0.0110 | 3.20 | 0.0111 | 3.21 | 0.0111 | 3.23 | 0.0112 | 3.25 | 0.0115 | 3.28 | 0.0115 | 3.28 |

| Sailplane | Toe-out Angle (deg) | | | | | | | | | | | |
|-------------------|---------------------|------|--------|------|--------|------|--------|------|--------|------|--------|------|
| | 0 | | -1 | | -2 | | -3 | | -4 | | -5 | |
| Dihedral (deg) | Cdi | AoA | Cdi | AoA | Cdi | AoA | Cdi | AoA | Cdi | AoA | Cdi | AoA |
| 0 | 0.0111 | 3.22 | 0.0112 | 3.2 | 0.0113 | 3.2 | 0.0114 | 3.2 | 0.0115 | 3.24 | 0.0117 | 3.24 |
| 15 | 0.0109 | 3.18 | 0.0110 | 3.19 | 0.0111 | 3.20 | 0.0112 | 3.21 | 0.0113 | 3.22 | 0.0115 | 3.23 |
| 30 | 0.0108 | 0.16 | 0.0109 | 3.17 | 0.0110 | 3.18 | 0.0111 | 0.2 | 0.0112 | 3.21 | 0.0113 | 3.23 |
| 45 | 0.0108 | 3.14 | 0.0108 | 3.15 | 0.0109 | 3.17 | 0.0110 | 3.19 | 0.0111 | 3.21 | 0.0112 | 3.22 |
| 60 | 0.0108 | 3.14 | 0.0108 | 3.16 | 0.0109 | 3.17 | 0.0110 | 3.18 | 0.0111 | 3.21 | 0.0112 | 3.23 |
| 83 | 0.0109 | 3.17 | 0.0110 | 3.19 | 0.0111 | 3.20 | 0.0111 | 3.21 | 0.0113 | 3.26 | 0.0113 | 3.26 |

